Correspondence to:
L. Berčič,
laura.bercic@obspm.fr

The Interplay Between Ambipolar Electric Field and Coulomb Collisions in the Solar Wind Acceleration Region

L. Berčič[1,2] [ORCID], **S. Landi[1,3]**, and **M. Maksimović[2]**

[1]Physics and Astronomy Department, University of Florence, Firenze, Italy, [2]LESIA, Observatoire de Paris, PSL Research University, CNRS, UPMC Université Paris 6, Université Paris-Diderot, Meudon, France, [3]INAF-Osservatorio Astrofisico di Arcetri, Firenze, Italy

Abstract The solar wind protons are accelerated to supersonic velocities within the distance of 10 solar radii from the Sun, as a consequence of a complex physical mechanism including particle kinetic effects as well as the field-particle energy and momentum exchange. We use a numerical kinetic model of the solar wind, accounting for Coulomb collisions (BiCoP), and model a solar wind accelerated only by the *ambipolar* electrostatic filed (E) arising due to the difference in mass between electron and proton, and assuring quasi-neutrality and zero current. We study the effect E, which was found to be on the order of Dreicer electric field (E_D) (Dreicer, 1959), has on the resulting electron velocity distribution functions. The strahl electron radial evolution is represented by means of its *pitch-angle width* (PAW), and the *strahl parallel temperature* ($T_{s,\parallel}$). A continuous transition between collisional and weakly collisional regime results in broader PAW, compared to the single-exobase prediction imposed by the exospheric models. Collisions were found to scatter strahl electrons below 250 eV, which in turn has an effect on the measured $T_{s,\parallel}$. A slight increase was found in $T_{s,\parallel}$ with radial distance, and was stronger for the more collisional run. We estimate that the coronal electron temperature inferred from the observations of $T_{s,\parallel}$ in the solar wind, would be overestimated for between 8% and 15%.

1. Introduction

The solar wind is a continuous flux of magnetized plasma which originates in the solar corona and permeates the interplanetary space. The first physical model explaining its existence was proposed by Parker (1958) in a form of a fluid hydrodynamic flow. The mass conservation of solar wind expansion results in a strong radial gradient in plasma density, decreasing with radial distance as r^{-2}, and even faster in the solar wind acceleration region. The plasma that escapes the hot and dense, collision dominated solar corona, therefore significantly decreases in density and becomes almost collisionless, over a few solar radii (R_S). Frequently used measure of collisionality is the ratio between the mean-free path of the particles (λ) and the atmospheric density scale-height (H), called the *Knudsen number* (K_n). Values $K_n \ll 1$ are typical for the solar corona, while $K_n > 1$ marks the weakly collisional and collisionless regimes, where departures from a thermal equilibrium, Maxwellian particle velocity distribution function (VDF), are expected. Accordingly with the Parker (1958) model, the transition between the two regimes (defined with $K_n = 1$) lies at the radial distance of about $4\,R_S$ (Brasseur & Lemaire, 1977).

Kinetic *exospheric* solar wind models were developed, with a goal to provide a more detailed description of the solar wind expansion physics above the transition point ($K_n = 1$), referred to as the *exobase*. A common element of all the exospheric solar wind models is an explicit existence of the global electrostatic field, resulting from the difference in mass between electron and proton. The first proposed kinetic model by Chamberlain (1960) assumed that this electrostatic field is the Pannekoek-Rosseland electric field, arising in any gravitationally bound plasma in hydrostatic equilibrium (Pannekoek, 1922; Rosseland, 1924). As the solar wind is not in such equilibrium, the electric field was underestimated, resulting in a subsonic solar wind solution, called *the solar breeze*.

Due to their smaller mass and consequently larger thermal velocity, the electrons evaporate from the solar corona faster than the heavier protons. The arising global electric field, also referred to as the *ambipolar* electrostatic field (E), must thus assure the equality of electron and proton fluxes at all radial distances,

allowing the Sun to remain charge-free. The ambipolar electric field was used in succeeding exospheric models (Jockers, 1970; Lemaire & Scherer, 1970, 1971; Maksimovic et al., 1997; Pierrard et al., 1999; Zouganelis et al., 2004), producing supersonic wind that agrees well with the measured solar wind plasma moments.

Scudder (1996) showed that the value of E in the solar wind critical point, the radial distance at which the solar wind protons become supersonic, should be on the order of *Dreicer electric field* (E_D) (Dreicer, 1959). The electric fields of that size were found to cause the electron *runaway* in the context of fusion laboratory experiments, resulting in large currents (Dreicer, 1960). A theory describing the effect of E on the solar wind electron VDF was developed by Scudder (2019b), who proposes that the supra-thermal electrons result from the runaway mechanism. No observational evidence of E interacting with electron VDF were reported so far.

The benefit of a kinetic description of the solar wind is that it allows the existence of non-thermal VDFs, commonly observed in the solar wind for both protons and electrons. Observed solar wind electron VDFs are normally modeled with three components: the dense electron *core* takes up the low electron energies, while the high energies are represented by field-aligned beam-like electron *strahl* and the electron *halo* present in all directions (Feldman et al., 1975; Macneil et al., 2020; Maksimovic et al., 2005; Pilipp et al., 1987; Štverák et al., 2008, 2009; Tao et al., 2016; Wilson et al., 2019a, 2019b). In exospheric models the velocity space at any radial distance is separated by the velocity required for an electron to escape from the potential well of the ambipolar electric field. Electrons with velocities smaller than the escape velocity can belong to either trapped, ballistic or incoming exospheric particle class, and are equivalent to the core component. Electrons with velocity high enough to escape, belong to the escaping class, and correspond to the strahl component (Lemaire & Scherer, 1971). The halo component is not present in the exospheric models, and is thus believed to be created through the electromagnetic (EM) field-particle interaction during the solar wind expansion, or exist already deep in the solar corona (Pierrard et al., 1999).

In the collisionless approximation the anti-sunward moving strahl electrons focus around the radially decreasing magnetic field, following the magnetic moment and energy conservation. However, the strahl observed in the solar wind was reported to broaden with radial distance (Berčič et al., 2019; Graham et al., 2017; Hammond et al., 1996), requiring the existence of strahl scattering mechanisms. Coulomb collisions were found to be efficient in isotropizing the electron core (Salem et al., 2003; Štverák et al., 2008), but have a much smaller effect on the higher energy electrons. A study of the Coulomb scattering of the strahl electrons using kinetic theory is presented in works by Horaites et al. (2018, 2019), who provide an analytical expression relating the *strahl pitch-angle width* (PAW) to the energy and density of solar wind electrons. PAW was found to decrease with electron energy, at 1 au affecting electrons below ∼300 eV. Proposed scattering mechanisms, effective at higher electron energies, include wave-particle interactions (Jagarlamudi et al., 2020; Kajdič et al., 2016; Verscharen et al., 2019; Vocks et al., 2005) and scattering by the background turbulence (Pagel et al., 2007; Saito & Gary, 2007).

Collisionless focusing in the absence of any field-particle interactions, does not affect the shape of the parallel profile of the strahl VDF ($f_{s,\parallel}$). This argument was used in the works by Hefti et al. (1999); MacNeil et al. (2017); and Berčič et al. (2020), trying to relate the temperature of the supra-thermal electron components to the coronal electron temperature at their origin. The study by Berčič et al. (2020), including the analysis of data from Parker Solar Probe (PSP) and Helios missions, reveals that the *strahl parallel temperature* ($T_{s\parallel}$), defined with a Maxwellian fit to the $f_{s,\parallel}$, does not vary with radial distance. Together with the found anti-correlation between $T_{s\parallel}$ and the solar wind speed, the authors conclude that the strahl does carry the information about the state of the electron VDF in the solar corona.

The results presented in this work were obtained using a numerical kinetic model of the solar wind expansion accounting for Coulomb collisions (Landi & Pantellini, 2001, 2003; Landi et al., 2010, 2012, 2014). The model does not capture all of the solar wind physics, but instead allows a detailed view into a kinetic behavior of the colliding solar wind electrons in the near-Sun regions.

Other existing models provide either numerical or analytical solutions of the drift-kinetic equation of the solar wind electrons, and account for scattering by Coulomb collisions (Boldyrev & Horaites, 2019; Held et al., 2003; Lie-Svendsen & Leer, 2000; Smith et al., 2012; Tang et al., 2018). All models require some
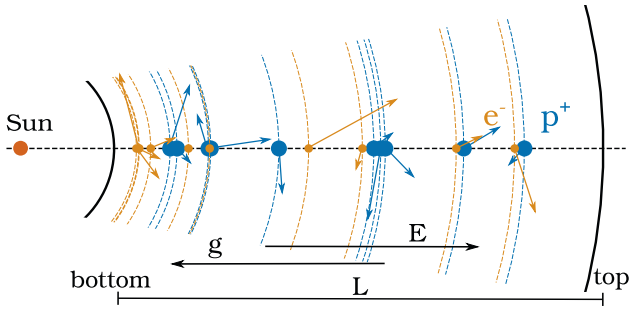
Figure 1. A schematics of the BiCoP model. The same amount of electrons (yellow) and protons (blue) moves in one dimension, which is aligned with the radial direction. The particles' velocities are defined in 3-dimensional space and represented by arrows in the schematics. We marked the two simulation boundaries and the directions of two fields acting upon the particles: the gravitational and the electric field. BiCoP, binary Collisions in Plasmas.

simplifications, for example, linearization of the collisional operator, or ad-hoc Maxwellian VDFs for the ions with prescribed density and temperature profiles, used in some of the works listed above. In binary Collisions in Plasmas (BiCoP) both electrons and ions are evolved kinetically, the system builds its own macroscopic quantity, and the ambipolar electric field self-consistently. Particles finding themselves on the same position in the simulated domain collide, with a cross-section corresponding to Coulomb collisions. More details about the model are given in Section 2. Since the global solar wind dynamics depends strongly on the characteristics of particle collisions, BiCoP provides a unique and self-consistent calculation of the ambipolar electric field, and accounts for natural transition from collisional to weakly collisional regime.

The modeled solar wind and its evolution through the acceleration region is described with plasma moments in Section 3. The analysis of the obtained electron VDFs permits an investigation of the effects of the ambipolar electric field on the VDFs (Section 4), and of the radial evolution of the strahl electron component (Section 5).

2. Numerical Model

We use the fully kinetic model BiCoP to simulate the radial expansion of the solar wind. Details of the model are described by Landi and Pantellini (2001, 2003), who in the first work present the evolution of solar wind moments over the first 0.2 R_S above the solar surface. In the second work they extend their simulation domain to reach up to 50 R_S, however, with decreased proton to electron mass ratio. Later works with BiCoP use realistic solar wind characteristics, like proton-electron mass ratio and the input plasma moments, and present the radial evolution of electron VDF between 0.3 and 3 R_S, where the solar wind has already reached its terminal velocity and the effect of gravity can be neglected (Landi et al., 2012, 2014). They show that the model produces a two-component electron VDF function - consisting of the core and the strahl, and the global solar wind moments which compare well with the observed values. With the evolution of the code as well as computer technology we are now able to conduct the simulations of the solar wind acceleration region where the effect of gravity is of great importance (1 R_S–49 R_S) using real proton to mass ratio and reproducing the plasma moments measured by the Parker Solar Probe (Fox et al., 2016).

A schematics of the simulation setup is shown in Figure 1. The model is 1-dimensional in space and 3-dimensional in velocity space. N macroparticles are included in the simulations representing two species – electrons and protons, defined by their opposite signed charge and realistic mass ratio ($\frac{m_p}{m_e} = 1837$). The particles are accelerated by the Sun's gravitational force and the ambipolar electric field force:

$$\frac{d^2 r}{dt^2} = -\frac{GM_S}{r^2} + \frac{\bar{L}^2}{m_i^2 r^3} + \frac{q}{m_i} E(r), \tag{1}$$

where, r is the radial distance from the Sun, G is the gravitational constant, M_S is the mass of the Sun, m_i is the mass of a particle, and $E(r)$ is the ambipolar electric field. $\bar{L}$ is the angular momentum that can be expressed in terms of perpendicular particle velocity: $\bar{L} = m_i \vec{r} \times \vec{v}$. In the model we assume a radial magnetic field so that angular magnetic conservation is equivalent to the magnetic moment conservation (Landi et al., 2012).

The main parameter defining the behavior of the system is the ratio between the gravitational potential and the electron thermal energy at r_0, the distance from the Sun's center and the simulation bottom boundary:

$$\gamma = \frac{GM_S}{r_0} \cdot \frac{m_e}{2 k_B T_{e,bot}}, \tag{2}$$

where, $T_{e,\text{bot}}$ is the temperature of electrons at the bottom simulation boundary. Gravity is thus expressed as

$$g_0 = \gamma \frac{l}{r_0},\tag{3}$$

with l the length of the simulation domain.

A benefit of the described kinetic model is a self-consistent calculation of the ambipolar electric field. The electric field in the simulation is composed of two contributions. First is a global electric field, radially decreasing with r^2, keeping the balance between electron and proton fluxes. Second is the charge-neutralizing electric field, a local polarization field resulting from local charge imbalances (Landi & Pantellini, 2001). This field is obtained by considering each particle as a thin spherical conducting shell centered in the Sun, and calculating the local field of a system of conducting spherical plates (Landi & Pantellini, 2003).

The BiCoP model is unique for its statistical treatment of binary Coulomb collisions. When two particles find themselves on the same position along the dimension of the simulation, they can either suffer an elastic collision or pass each other undisturbed. The collision probability decreases with v^4, as predicted by Coulomb cross-section. To save the computational time particles with relative velocity lower than a defined velocity limit (v_C) will collide every time. Landi and Pantellini (2001) show that this computational simplification does not change the Coulomb collisions properties and have the same effect on the electron VDF as long as v_C is smaller than the thermal velocity of the electrons at any radial distance ($v_C < v_{\text{th}}$). Even more, we make use of this parameter to vary the collisionality of the system.

The one-dimensional simulation domain is limited by the bottom and the top boundary, of which the bottom boundary is located closer to the Sun. The shape of the proton and electron VDFs in these two points is defined with the input parameters $T_{e,p,\text{bot}}$, $T_{e,\text{top}}$. In the present study all the boundary VDFs are isotropic and Maxwellian-like, which leaves us with the temperature and the bulk velocity as the only free parameters. The bottom and top velocities are the same for both species (v_{bot}, v_{top}). We define the temperature of the both species at the bottom ($T_{e,\text{bot}}$, $T_{p,\text{bot}}$), and the temperature of electrons on the top ($T_{e,\text{top}}$), as the protons at the top have a supersonic velocity, thus all leaving the simulation domain and being re-injected at the bottom. On the contrary, electrons are subsonic, thus a portion of them has to be injected back from the top boundary with a probability and velocity which are given by the distribution function assumed at the top. The equal flux between the two species is assured everywhere in the system only by the self-consistent electric field. The kinetic model tends toward a stationary, quasi-neutral solar wind solution only if the boundary conditions are also a part of this solution. Therefore the choice of $T_{e,\text{top}}$ and v_{top} is not really free, and depends on the $T_{e,\text{bot}}$ and $T_{p,\text{bot}}$, as well as on the collisionality of the system. For each of the presented simulation runs, test runs were preformed iterating toward good values for the top boundary parameters.

The particle's velocity distribution functions are built by binning the spatial domain in 40 bins and the velocity space in 80×80 bins in the radial and perpendicular direction. Once the stationary state has been reached the position and velocity of the particles are regularly sampled to build the velocity distribution function as function of the distance. Moments of the distribution function are also directly computed in the simulation. The presented simulation runs with their key parameters are listed in Table 1.

3. Density, Velocity, & Temperature

3.1. Method

3.1.1. Physical Unit Density

Figure 2 shows the radial evolution of density (n), velocity (v), and core electron temperature ($T_{e,\text{core}}$) over the simulation domain for the four presented simulation runs. The physical units of the parameters in the equation of motion (Equation 1: r, v, T, E) are all determined through the mass, gravity and temperature of the corona. Particle density, however, does not affect gravitational and electric fields, but it plays an important role for the properties of Coulomb collisions. The physical units for density are thus determined using the electron-proton collision frequency ($\nu_{e,p}(r)$) measured in the simulation and comparing it to the

Table 1
Presented Simulation Runs and Their Crucial Input Parameters

Parameters	Unit	A	HC	MC	LC
N		22,500	22,500	22,500	22,500
v_C	$v_{th,0}$	0.4	**0.4**	**0.3**	**0.2**
$T_{e,p,bot}$	10^6 K	2	1.4	1.4	1.4
$T_{e,top}$	10^6 K	0.82	0.77	0.77	0.77
g_0		0.1416	0.0225	0.0225	0.0225
r	R_S	**1–46**	3–49	3–49	3–49
v_{bot}	km/s	0	104	104	104
v_{top}	km/s	218	228	228	228

Note: Where the key differences between simulation runs are marked in bold.
Abbreviations: HC, high collisionality; LC, low collisionality; MC, medium collisionality.

Fokker-Planck electron-proton transport collision frequency for a plasma with known density (n) and temperature (T):

$$n = \frac{v_{e,p} v_{th,0}}{l} \cdot \frac{3\epsilon_0^2 m_e^{1/2} (k_B T)^{3/2}}{4(2\pi)^{1/2} e^4} \frac{1}{ln\Lambda}, \tag{4}$$

where $v_{th,0}$ is the electron thermal velocity in the first radial bin and $ln\Lambda$ is the Coulomb logarithm:

$$ln\Lambda = ln\left(\frac{12\pi(\epsilon_0 k_B T)^{3/2}}{n^{1/2} e^3} \right). \tag{5}$$

Since the unknown density n is required for the calculation of $ln\Lambda$, we first obtain n' assuming $ln\Lambda = 24$ in Equation 4, which is close to expected value for resulting plasma parameters: $ln\Lambda(T = 172$ eV, $n = 10^6$ cm$^{-3}) = 24.3$, $ln\Lambda(T = 120$ eV, $n = 10^4$ cm$^{-3}) = 26.1$. The final density n_0 is 10 obtained by:

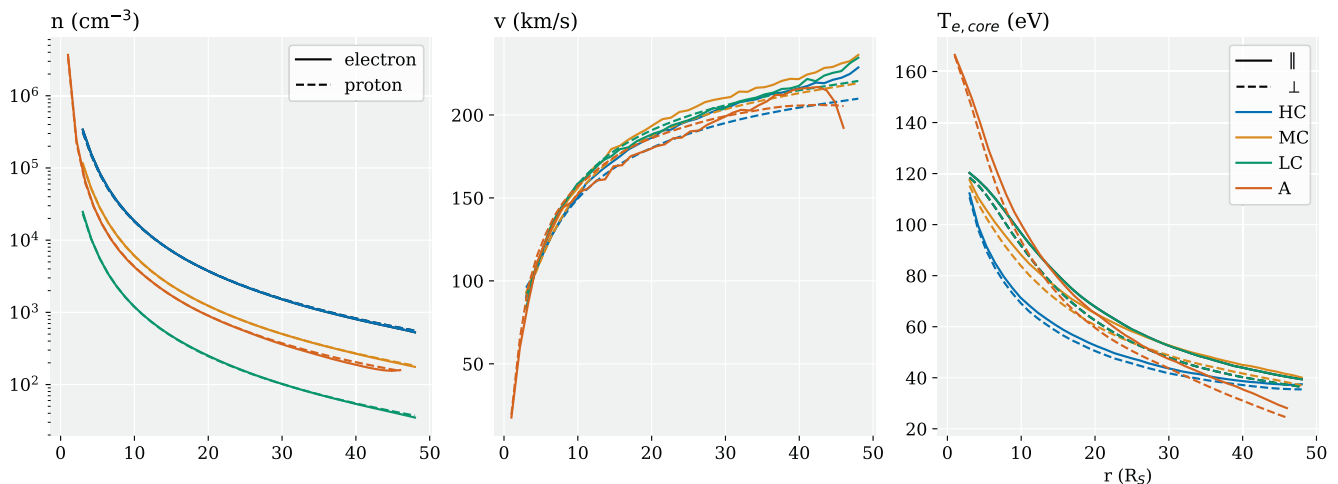$$n_0 = n' \frac{24}{ln\Lambda(n')}, \tag{6}$$

Figure 2. The evolution of electron and proton density (left), velocity (middle), and electron core parallel and perpendicular temperature (right) for all the presented simulations runs specified in Table 1.
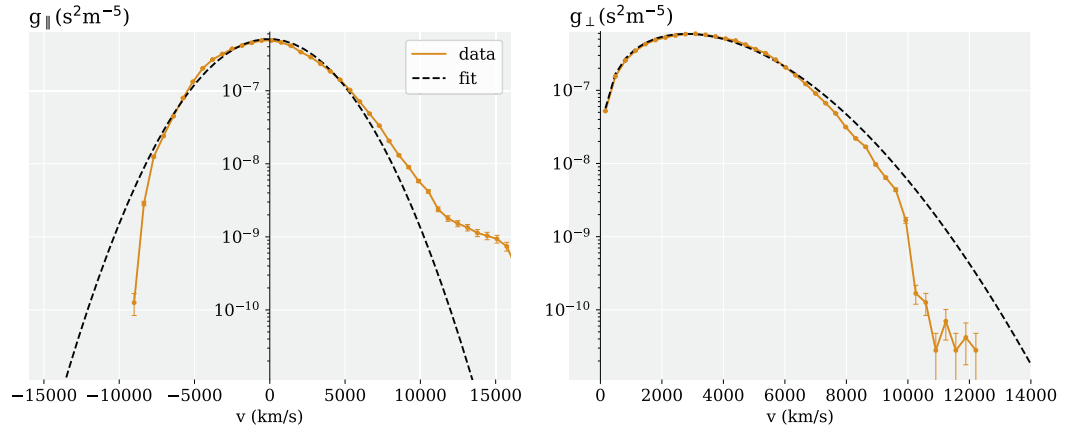
Figure 3. An example of a core fit to $g(v_\parallel, v_\perp)$, shown with the parallel (left), and the perpendicular (right) cut through electron VDF multiplied by $v_\perp$. Error bars represent the standard error for Poisson counting ($\sqrt{N}$). An example is taken from simulation run MC at the radial distance of 35 R_S. VDF, velocity distribution function.

The first radial bin is the densest and most collisional, thus n_0 is calculated there, and used to normalize the other radial bins accordingly with the number of particles they contain.

Simulation run A, the only presented run starting from $r_0 = 1R_S$, exhibits very strong gradients in density, velocity and temperature for its first three radial bins ($<3R_S$, see Figure 2). The Knudsen number, rises from $\sim 10^{-2}$ (first bin) to ~ 0.5 (third bin), remaining in the collisional regime. Because the collisionality continues to stay high in the third radial bin, the density there can be determined through the comparison with the Fokker-Planck collision frequency as well. However, the value obtained this way turns out to be an order of magnitude lower than the value calculated through normalization to the first radial bin. This gives us a high uncertainty on the calculated physical unit density. The accuracy could be improved by increasing the amount of particles used in the simulation, which would substantially increase the computation time. Instead, we decided to exclude the high-gradient region just above the solar surface and conducted our other presented simulation runs staring from $r_0 = 3R_S$. This way, the used amount of particles is sufficient to provide a good estimate of the physical unit density.

3.1.2. Core Electron Fit

Electron VDFs in the simulation are produced for each of the 40 radial bins, on a 2-dimensional cartesian grid (80,80) with a maximum velocity of $4v_{th,0}$. The output function $g(v_\parallel, v_\perp)$ is given in a form:

$$g(v_\parallel, v_\perp) = f(v_\parallel, v_\perp) \cdot v_\perp, \tag{7}$$

where $f(v_\parallel, v_\perp)$ is the velocity distribution function, and $v_\parallel$ and $v_\perp$ are the velocities parallel and perpendicular to the magnetic field (which is in the simulations purely radial). The lower energy part of $g(v_\parallel, v_\perp)$ is fitted with a bi-Maxwellian distribution function multiplied by $v_\perp$ (see Figure 3):

$$g_c(v_\perp, v_\parallel) = A_c \exp\left(\frac{v_\perp^2}{w_\perp^2} + \frac{(v_\parallel - \Delta v_\parallel)^2}{w_\parallel^2} \right) \cdot v_\perp, \tag{8}$$

where $\Delta v_\parallel$ is the drift velocity along the magnetic field, and the core density (n_c), and the core parallel and perpendicular temperatures can be obtained by:

$$n_c = A_c \cdot \pi^{3/2} w_\perp^2 w_\parallel, \tag{9}$$

Table 2
Electron Moments for Simulations HC, MC, and LC at 35 R_S

Moments	HC	MC	LC
n (cm^{-3})	1,129	376	76
v (km/s)	211	217	212
$T_{e,core,\parallel}$ (eV)	40.7	48.4	47.6
$T_{e,core,\perp}$ (eV)	39.0	44.6	43.3

Abbreviations: HC, high collisionality; LC, low collisionality; MC, medium collisionality.

$$T_{c\perp,\parallel} = \frac{m_e w_{\perp,\parallel}^2}{2k_B}. \qquad (10)$$

3.2. Results

Simulation run A starts at the solar surface where we set the input proton and electron VDFs to be isotropic Maxwellians with a temperature of 2 MK (172 eV) and zero bulk velocity (see Table 1). The density in the first radial bin reaches 4×10^6 cm^{-3} (see Figure 2). The density and velocity of both species are aligned verifying charge neutrality and mass flux conservation. Solar wind protons become supersonic at the distance of 4 R_S and reach their highest velocity of 218 km/s at 42 R_S. As mentioned in the previous section, due to high gradients in the first few radial bins we have a large uncertainty on the calculated density for the simulation run A. We show this run to prove that BiCoP can produce a supersonic wind from a static hot solar corona, and use the obtained temperature and velocity as a guidance for the input parameters for the runs high collisionality (HC), medium collisionality (MC), and low collisionality (LC) starting from 3 R_S. As mentioned above, $T_{e\&p,bot}$ and v_{bot} are not independent parameters, and a simulation starting with $T_{e\&p,bot} = 150$ eV, and $v_{bot} = 90$ km/s at 3 R_S, as follows from the simulation run A, does not result in a stationary solution. That is because the bottom boundary proton and electron VDFs (at 3 R_S) are set to be isotropic Maxwellians, however, in the simulation run A at this distance the VDFs are already deformed: protons appear anisotropic and electrons start to form a tenuous strahl population. Instead of changing the shape of the VDFs at the bottom boundary of the simulations starting at 3 R_S we decrease $T_{e\&p,bot}$ (to 120 eV). This way the radial evolution of v is similar for all runs, while there are some differences in the radial evolution of T.

Because the highest gradients are avoided for the runs HC, MC, and HC, the used amount of particles (22,500 electrons and 22,500 protons) provides us with much better statistics. We study the effect of Coulomb collisions by varying the system collisionality using the input variable v_C. Run HC is the most collisional ($v_C = 0.4$), which is reflected in higher density and steeper decrease in core electron temperature with radial distance (see Figure 2). The core stays close to isotropic all through the simulation domain, while in less collisional runs MC ($v_C = 0.3$) and LC ($v_C = 0.2$), the parallel core electron temperature is notably larger than the perpendicular one. The collisionality does not appear to have an effect on the final solar wind velocity, which is similar for all three runs, ∼220 km/s. This result is in contradiction with the simulation results shown by Landi and Pantellini (2003), who found that denser solar wind is accelerated to higher velocities. The discrepancy between the two results could be a consequence of the reduced proton to electron mass ratio, or much smaller amount of particles used in the simulation runs from Landi and Pantellini (2003).

For a quantitative comparison of the obtained electron moments with the Parker Solar Probe data we list the simulation values at 35 R_S in Table 2.

4. Electric Field and Electric Potential

4.1. Method

Another simulation output is the ambipolar electric field (E) at the position of every simulation particle. These values are then binned accordingly with the 40 radial bins and integrated over radial distance to obtain the electric potential (ϕ).

In the exospheric solar wind models, the total electric potential difference between any given distance and infinity has an important effect on the electron VDF. At any radial distance (r) the antisunward moving electrons with the energy higher than the electric potential energy ($\mathcal{E}_\phi(r)$) are able to escape and form the strahl population, while electrons with energy below $\mathcal{E}_\phi(r)$ cannot escape and form a ballistic, core population. The antisunward core electrons are trapped in a potential well: they advance up to a distance where their radi-
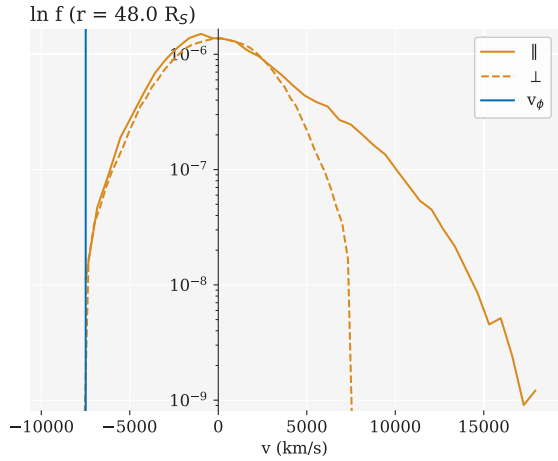
Figure 4. Parallel and perpendicular cuts through electron VDF, in the last radial bin of the simulation run MC, at a distance of 48 R_S, plotted in the *Sun's rest frame*. The negative cutoff velocity is marked with a blue line. VDF, velocity distribution function.

al velocity becomes zero, and then start falling back toward the Sun, at every distance reaching the same absolute velocity as on the way up, only in the opposite direction. The velocity of electrons with the energy $e\phi$:

$$v_\phi(r) = \sqrt{\frac{2e\phi(r)}{m_e}},$$ (11)

thus represents a boundary in the sunward direction, the cutoff velocity below which no electrons are found. v_ϕ is defined in the Sun's rest frame.

The electric potential difference obtained in the simulation is not the total electric potential supposed to be present in the solar wind, but the potential difference between a given radial distance and the top simulation boundary ($\Delta\phi(r) = \phi_{\text{top}} - \phi(r)$). To obtain the total electric potential, and not only the potential over the simulation length, we estimated the potential difference between the top boundary and infinity, or interstellar medium ($\phi_{\infty-\text{top}}$). The ambipolar electric field is the strongest close to the Sun where the solar wind acceleration is the fastest, and decreases with radial distance with a power law between 1 and 2. Therefore $\phi(r)$ asymptotically approaches zero for large radial distances and $\phi_{\infty-\text{top}}$ is relatively small.

Fist we estimated $\phi_{\infty-\text{top}}$ from the electron VDF in the last radial bin. We use the exospheric model prediction and look for the cutoff electron velocity in the sunward direction (see Figure 4). Technically this cutoff velocity is determined by the electron VDF prescribed at the upper boundary ($T_{e,\text{top}}$). Even though $T_{e,\text{top}}$ is an input parameter, it is dependant on the conditions set at the bottom boundary, and was found trough iteration toward a stationary solution conserving fluxes of both species. As $T_{e,\text{top}}$ is the same for runs HC, MC and LC, so is the cutoff velocity in the last radial bin: $v_{\phi,\text{top}} = -7,490$ km/s. This velocity corresponds to electric potential $\phi_{\infty-\text{top}} = 159$ V.
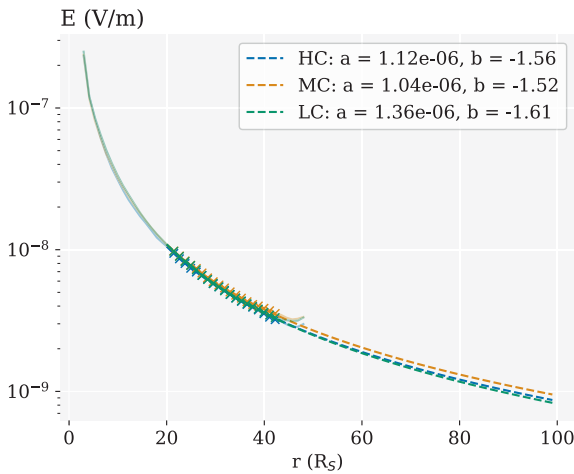

Figure 5. The extrapolation of E above the top simulation boundary. E measured in the simulation runs HC, MC and LC is shown with a pale full line, crosses denote the points used for the fitting with Equation 12, and the dashed lines the fitted curves. The obtained fitting parameters are shown in the legend. HC, high collisionality; LC, low collisionality; MC, medium collisionality.

The estimation of $\phi_{\infty-\text{top}}$ can also be found from the radial extrapolation of E measured in the simulation runs. To predict the behavior of E for the distances above the top boundary, existing values were fitted with a power law function:

$$f_E(r) = a \cdot r^b,$$ (12)

where a and b are the fitting parameters. The fit was performed only to the points above the distance of 21 R_S to avoid regions of strong solar wind acceleration. Acceleration contributes to the total value of E, and only above the acceleration region we expect for E to evolve as a power law with the radial distance. An upper radial distance limit was set to 44 R_S, to avoid the effects of the simulation upper boundary. The results of the fitting procedure are shown in Figure 5, where the fitted values are marked by crosses and the dashed line represents the obtained fit for each of the three simulation runs. The obtained fitting parameters (a and b) are marked in the legend. $\phi_{\text{top},\infty}$ is then obtained by integration of Equation 12 on the interval between 49 R_S and ∞. The resulting $\phi_{\text{top},\infty}$ are very close to the one estimated from electron VDF, amounting to 159, 181, and 144 V, for simulation runs HC, MC, and LC, respectively.

Even though $\phi_{\text{top},\infty}$ is not a direct output of the simulation, we are confident in the obtained values, as the two different estimation approaches give very similar results. For simplicity, the value $\phi_{\infty-\text{top}} = 159$ V obtained from electron VDFs, is used in further analysis.

The absolute value of ambipolar electric field obtained by the simulation is compared to the Dreicer electric field (E_D) (Dreicer, 1959), a measure of electric field strength required for an electron with a kinetic energy of $\frac{3}{2} k_B T_e$ to gain the energy of $k_B T_e$ in one mean-free-collision time. E_D is defined as:

$$E_D = \frac{k_B T_{e,core}}{e \lambda_{mfp}}, \tag{13}$$

where λ_{mfp} stands for the mean-free path, which is calculated as the ratio of electron thermal velocity ($v_{e,th}$) and electron—proton collision frequency ($\nu_{e,p}$) measured in the simulation.

Following the works of Fuchs et al. (1986) and Scudder (1996), the electron velocity space can be separated into two regions by a boundary velocity defined as:

$$v_D = \sqrt{\frac{3 k_B T_{e,core}}{m_e} \cdot \frac{2 E_D}{E}}, \tag{14}$$

where, E is the total, ambipolar electric field. Electrons with velocity lower than v_D defined in the ion rest frame, collide frequently enough for the electric force to be overdamped with Coulomb collisions, preserving a Maxwellian shaped VDF. Electrons with velocity higher than the defined boundary are underdamped by collisions and experience an acceleration by the electric force, becoming the so called, runaway electrons.

4.2. Results

The radial evolution of electric potential (ϕ) and electric field (E) is shown in Figures 6a and 6b. While both of these quantities remain very similar for the three simulations, a strong variation is seen for the Dreicer electric filed (E_D), a parameter comparing electric field with the collisionality of the system. Accordingly, the ratio E/E_D reaches the highest values for the least collisional case (~ 20 in run LC), and stays on the order of 1 for the most collisional case (run HC, Figure 6c). Figure 6d shows the velocity v_D defined in the previous section, separating the over- and underdamped regions of the VDF.

Expected uncertainties of the parameters in Figure 6 are not displayed, as they are relatively small and uniform over radial distance. Standard Poisson counting errors for ϕ and E are obtained as $\sqrt{N}$, where N is the number of particles used for a calculation of ϕ and E at each radial distance. They vary between 3% and 5%. The uncertainties of parameters E_D and v_D depend also on the errors of $T_{e,core}$ resulting from fitting. These were found to be smaller than 1%. We can safely conclude that our results are not strongly affected by statistical uncertainties.

We compare the calculated separation velocities v_ϕ and v_D with the measured electron VDFs. A new representation method introduced by Behar et al. (2020) is used to highlight higher order VDF features and their departures from isotropy. Left plot in Figure 7 displays an original gyrotropic VDF from the simulation run MC. A 2-dimensional linear interpolation between the sampled points was used, resulting in a smoother and more continuous plot. Logarithmic color scale allows a recognition of the typical electron VDF features: a dense and isotropic core component and a beam-like strahl at positive velocity values. The middle plot shows the same VDF in the *scaled* representation, where each energy bin—each circular belt in the ($v_\parallel$, $v_\perp$) parameter space—is scaled to the values between 0 and 1. With this representation we lose the information about the absolute value of f and its strong gradient along the energy dimension, but we expose the smaller anisotropic features at all energies. In cases where two features arise in the same energy bin, the scaled VDFs can be misleading, only highlighting the bigger feature. The right plot shows the normalized representation, where the values are normalized to the perpendicular cut through electron VDF ($f_\perp = f(v_\parallel = 0)$). Regions of VDF where the density flux is lower than along the perpendicular direction appear in blue and regions with higher density in red. With this representation the small VDF features are less pronounced than in the scaled VDF, however a relation with the original VDF is preserved through a norm, in this case chosen to be $f_\perp$. VDFs are shown in electron core resting frame, as this is the frame in which isotropy is expected.
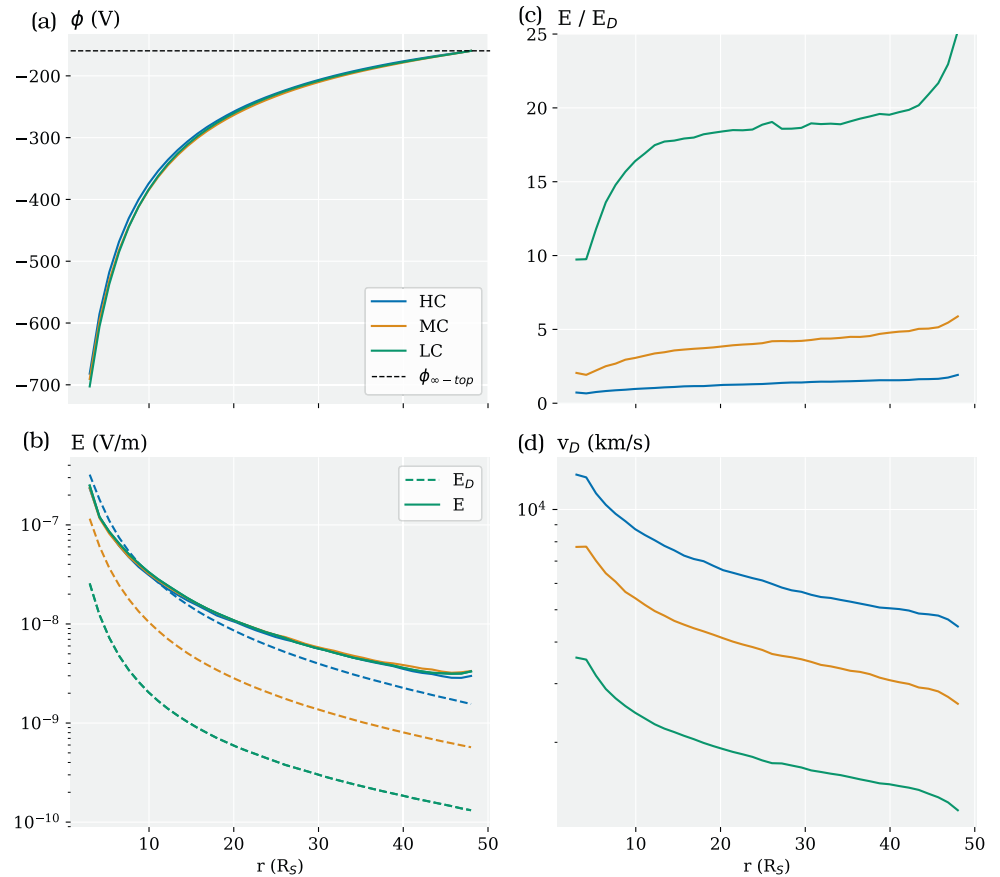
Figure 6. (a) Electric potential measured in the simulations and shifted for the estimated potential above the top simulation boundary ($\phi_{\infty-top}$), (b) Ambipolar electric field (E) (full line) and Dreicer electric field (dashed line), (c) The ratio between ambipolar and Dreicer electric field, (d) separation velocity (v_D).

The scaled distribution reveals two features aligned with magnetic field: the strahl present at positive velocities, and another overdensity at small negative velocities. The second feature is very small and does not appear in the normalised representation. It results from a slight mismatch between the anti-sunward portion of electron VDF leaving the simulation at the top boundary and the sunward portion defined with input parameters.

v_D and v_ϕ are overplotted as half circles with dashed black, and full blue line, respectively. Positive signed v_D corresponds to the velocity where first strahl electrons are found (see the scaled representation), while negative signed v_ϕ coincides with the cutoff, clearly seen in blue in the normalised representation. Since electron core is close to isotropic and drifting with a relatively low speed, positive signed v_ϕ also corresponds to the upper velocity limit of the core population. The same conclusions follow from the electron VDF slices at two different radial distances shown in Figures 8a and 8b.

We are interested in the behavior of electron VDF parallel to the magnetic field, thus we average the values within a pitch-angle 10° to create parallel cuts through the VDF in original, scaled and normalised representation. These values are then plotted with respect to the radial distance in Figure 9, for the simulation run MC. This plotting technique allows us to observe the radial evolution of the core and the strahl component. Over all radial distances positive v_D follows the transition between the core and the strahl component (see scaled representation), while negative v_ϕ follows the exospheric cutoff (see normalised representation). The same type figures for simulation runs HC and LC are added in Appendix A.

We compare the cuts through electron VDF at the same radial distance, in three different simulations in Figures 8b–8d. The first notable difference is the break-point velocity between the core and the strahl electrons.
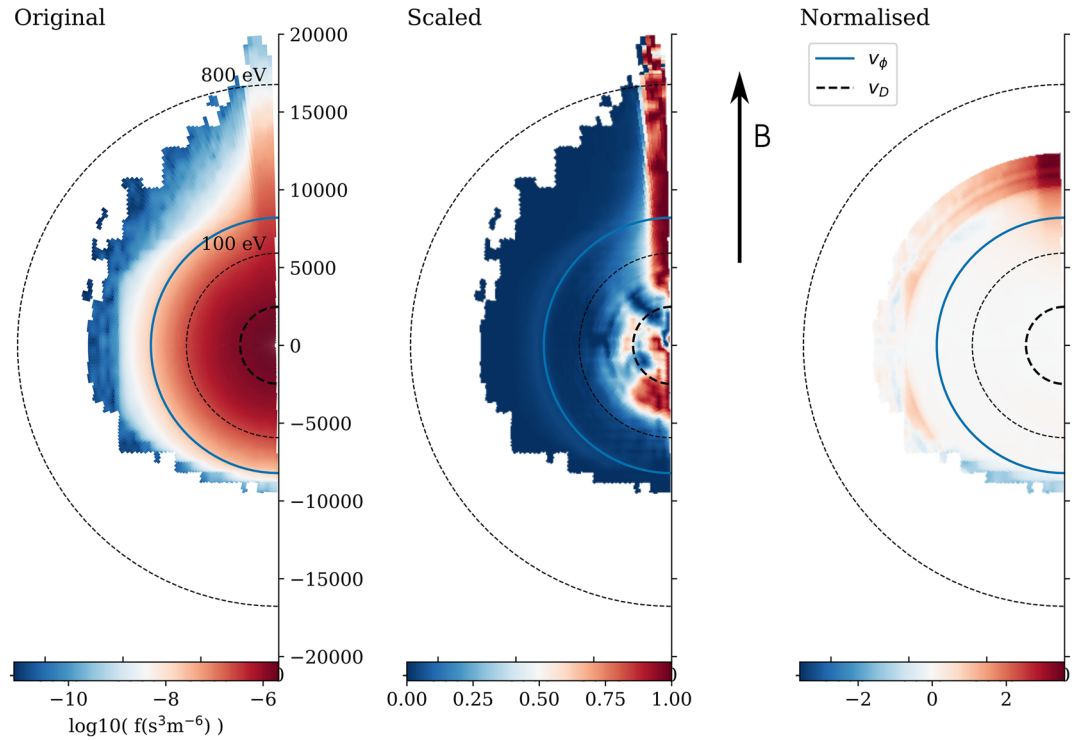
Figure 7. Two-dimensional representation of a gyrotropic electron VDF in the 28th radial bin (35 R_S) of the simulation run MC. The original electron VDF is shown on the left, a scaled VDF in the middle, and a normalised VDF on the right. We use the core electron resting frame where magnetic field is aligned with the y-axis. The electric potential velocity (v_ϕ) and the Dreicer velocity (v_D) are marked with blue and black lines. MC, medium collisionality; VDF, velocity distribution function.

In the more collisional run HC the collisions are able to maintain a Maxwellian VDF up to higher velocity compared to the less collisional runs MC and LC. While v_ϕ is almost the same for all the runs, v_D reflecting the collisionality of the system varies between the runs.

Both, positive and negative signed velocities v_ϕ and v_D, are marked on all plots because they are expected to describe the VDF in both senses. In the antisunward direction $v_\phi > v_D$ means that the electrons with energies smaller than the local potential energy, which will eventually be slowed down and start falling back toward the Sun, already exhibit non-Maxwellian features. Whether this results in a non-Maxwellian sunward directed portion of electron VDF cannot be determined with the results obtained from our model. The sunward portion of the VDF is defined at the top boundary and is assumed to be Maxwellian.

5. PAW and Strahl Parallel Temperature ($T_{s,\parallel}$)

5.1. Method

We define the strahl as the residual anti-sunward component of the electron velocity distribution function and we characterize it with two parameters, the PAW and the *strahl parallel temperature* ($T_\parallel$), in the same way as in the observational studies by Berčič et al. (2019, 2020). PAW width is obtained as a full width half maximum of the pitch-angle distributions in an energy bin:

$$f_i(\alpha) = f_{max,i} \cdot \exp\left(-\frac{\alpha^2}{2\sigma_i^2}\right), \qquad PAW_i = 2\sqrt{2\ln 2} \cdot \sigma_i, \tag{15}$$
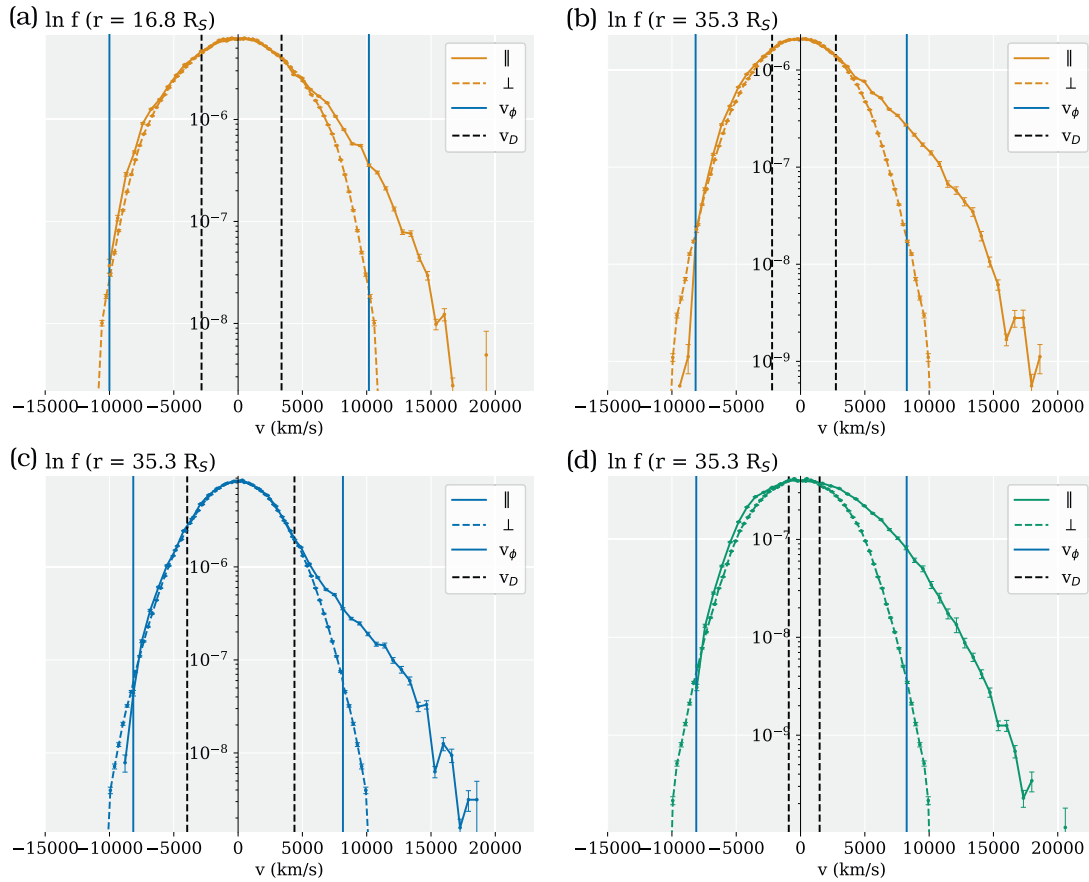
Figure 8. Parallel and perpendicular cuts through an electron VDF at the distance of 17 R_S (a) for the simulation run MC, and at 35 R_S (right) for the simulation runs HC (c), MC (b), and LC (d). The cuts are plotted in core electron resting frame. v_ϕ and v_D are indicated with blue and black lines. Error bars represent the standard error for Poisson counting ($\sqrt{N}$). HC, high collisionality; LC, low collisionality; MC, medium collisionality; VDF, velocity distribution function.

where, α is the pitch angle and index i denotes different energy bins. We arbitrarily define 20 logarithmically spaced energy bins between energies 79 and 3,162 eV. Logarithmic spacing was used to provide a better comparison between the simulation and observational data, as electrostatic analyzers normally sample electron energies in this way.

$T_{s,\parallel}$ is obtained by fitting a one-dimensional Maxwellian to the VDF integrated along the perpendicular direction ($f_\parallel = \int f(v_\parallel, v_\perp) dv_\perp$) in the logarithmic space:

$$\ln f_\parallel(v_\parallel) = -\frac{m_e}{2 k_B \cdot T_{s\parallel}} \cdot v_\parallel^2 + \ln\left(n_s \sqrt{\frac{m_e}{2\pi k_B \cdot T_{s\parallel}}} \right). \tag{16}$$

The fit is performed only to the antisunward portion of electron velocity space dominated by the strahl electron population (see Figure 10). We found that v_ϕ in the sunward and anti-sunward direction describes well the properties of the electron core. Therefore, we use it as the separation velocity between the core dominated and strahl dominated portions of electron VDF. An upper energy limit for the energies included in the $T_{s,\parallel}$ fit was arbitrarily set to 1,274 eV to avoid inclusion of the noise.

5.2. Results

The comparison of PAWs at the radial distance of 35 R_S for the three simulation runs shown in Figure 11 reveals that Coulomb collisions only affect the lower energy strahl electrons. The first plotted PAW value denotes the energy at which the PAW of the electron VDF drops below 180°, marking the boundary between
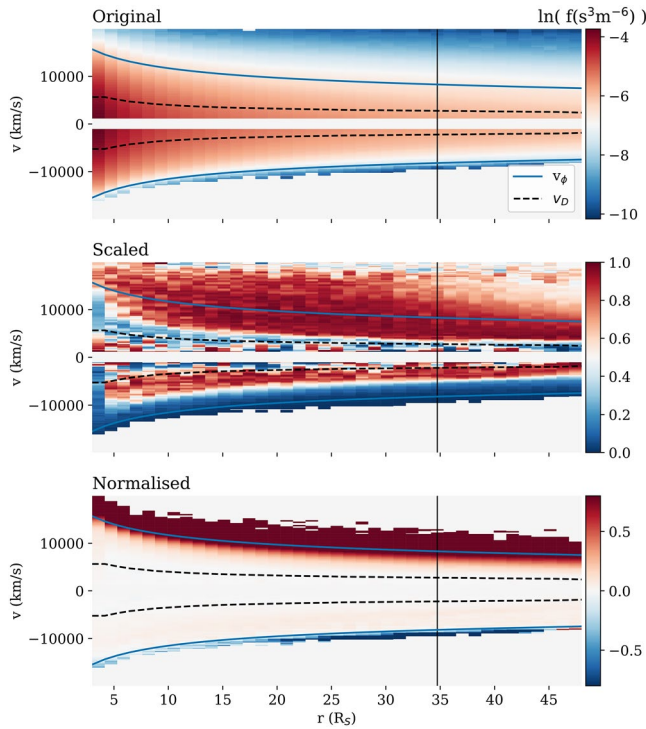
Figure 9. Parallel cuts through electron VDF plotted with respect to the radial distance in original (top), scaled (middle), and normalised (bottom) representation for the simulation run MC. v_ϕ and v_D are marked with blue and black lines. A black vertical line denotes the radial distance of the VDFs shown in Figures 7 and 8 (right). VDF, velocity distribution function.

the core and the strahl electrons. The strahl break point energies are different for the three runs, as already observed from VDF slices (Figure 8). The PAWs also exhibit different shapes with respect to the electron energy: the transition between broad strahl at lower electron energies, and narrow strahl at high energies is smoother for the more collisional case HC, and more abrupt for the less collisional cases MC, and LC. Above $\sim$250 eV three PAW curves reach the same value, showing that collisionality of the system does not affect the high energy electrons.

Results of the collisionless single-exobase focusing model (see Equation 6 in Berčič et al., 2019) are also shown in Figure 11 for two different sets of input parameters. The red dashed line shows the PAW obtained at 35 R_S if the exobase (r_0) is set to 3 R_S and the potential difference $\Delta\phi = 700$ V (like in BiCoP runs). As it results on still much narrower strahl, we increased the exobase and decreased the potential difference accordingly. The result of a simple model that matches well PAWs obtained from all three simulation runs above $\sim$250 eV, and the least collisional run LC down to the energy $\sim$130 eV, was found for $r_0 = 10 R_S$, and $\Delta\phi = 400$ V.

Our results are compared to the analytical solution for the width of the strahl provided by Boldyrev and Horaites (2019), Equation 18. The variables needed in Equation 18 were taken from simulation run MC. T_0, r_0, n_0, and Λ refer to the bottom simulation boundary at 3 R_S, and the strahl width was calculated at the radial distance 35 R_S. The authors solve the drift-kinetic equation accounting for Coulomb collisions using a collisional operator. Their solution corresponds well to the BiCoP most collisional run (HC).

The black dashed line shows PAW values measured in the low electron beta solar wind (<0.7) during the second encounter of PSP, shown in Berčič et al. (2020)—Figure 5b. The observed strahls appear 10–20° wider for the high electron energy part, but show a smooth transition between broad and narrow strahl, similar to the one found in the simulation run HC. The strahl break point found from PSP data appears at lower energy compared to the run HC, but correlates well to the break point found for run MC.
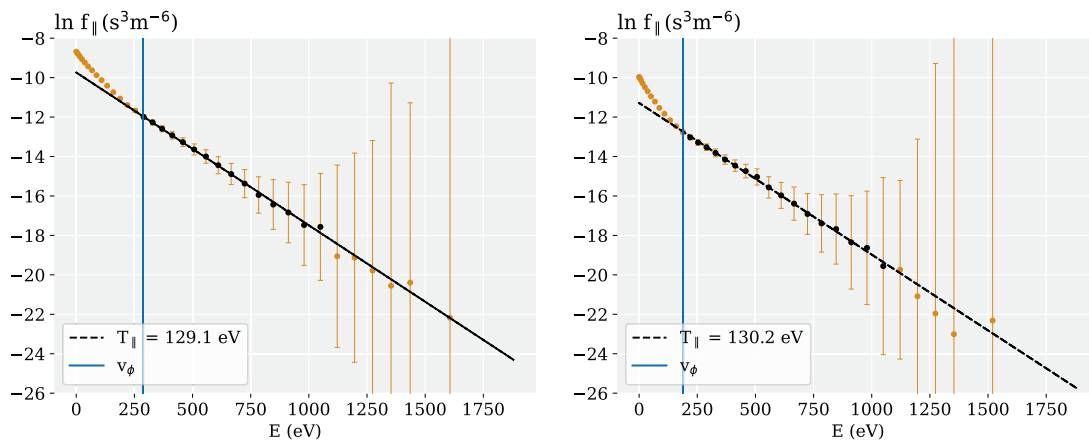
Figure 10. An example of the Maxwellian fit to the parallel strahl VDF ($f_\parallel$) to obtain $T_{s,\parallel}$, shown for simulation run MC at radial distances 17 R_S (left), and 35 R_S (right). The data points not included in the fit are marked with yellow and the data points included in the fit with black. The black dashed line shows the fit with the resulting $T_{s,\parallel}$ marked in the legend, and the blue line denotes the assumed separation velocity between the core and the strahl component. Error bars represent the standard error for Poisson counting ($\sqrt{N}$). VDF, velocity distribution function.

Figure 11. Strahl PAWs shown for electron VDFs at the radial distance of 35 R_S for the simulation runs HC, MC and LC. Error bars represent the standard error for Poisson counting ($\sqrt{N}$). The colored dashed lines show PAWs obtained from collisionless single-exobase focusing model for different choices of the exobase (r_0). Averaged PAW observed during the first two encounters of PSP in the low electron beta solar wind is shown with a black dashed line and 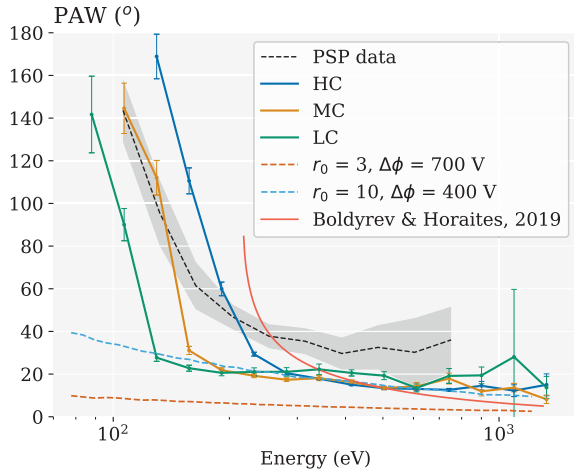a gray belt denoting the measurement error. The observational data was taken from Berčič et al. (2020). Red line represents the analytical solution from Boldyrev and Horaites (2019), Equation 18. HC, high collisionality; LC, low collisionality; MC, medium collisionality; PAW, pitch-angle width; VDF, velocity distribution function.
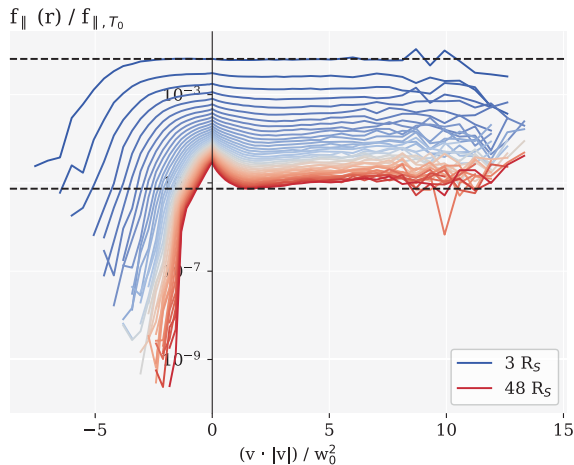
An increase of $T_{s,\parallel}$ with radial distance was found in all three simulation runs. Figure 12 shows electron VDFs integrated along the perpendicular direction ($f_\parallel$) at different radial distances normalised with a integrated Maxwellian VDF defined at the bottom boundary ($f_{0,\mathrm{Maxw}}$):

$$l = \frac{\int f_i(v_\parallel, v_\perp) dv_\perp}{\int f_{0,Maxw}(v_\parallel, v_\perp) dv_\perp}, \tag{17}$$

where index i is the number of the radial bin. This technique was used to verify the exospheric prediction, which says that $f_\parallel$ should, in absence of collisions and wave-particle interactions, remain unchanged in the exosphere, and carry the information about the shape of the VDF at the exobase to farther radial distances. If $T_{s,\parallel}$ remains unchanged from the bottom boundary the presented normalization results in a horizontal line, as found for the VDF in the first radial bin (blue color). Decreasing curves denote temperatures smaller than $T_{e,\mathrm{bot}}$, which can be seen for farther radial distances (red color) at low electron energies and represent the electron core population. Increasing curves appearing at strahl electron energies indicate that the $T_{s,\parallel}$ slightly increases with radial distances. Figure 12 includes values from the run MC, while plots for runs HC and LC are added in Appendix B.

The same result was obtained by fitting $f_\parallel$ with a 1D Maxwellian to obtain $T_{s,\parallel}$ (see Figure 13). The increase in $T_{s,\parallel}$ is the largest for the most collisional run A, at radial distance of 35 R_S by 15% exceeding the initial $T_{e,\mathrm{bot}}$. The smallest increase was found in run C, amounting to 3%.

6. Discussion

6.1. Modeled and Observed Solar Wind

The used kinetic solar wind model does not capture all the physics of the solar wind. Most importantly it does not account for electro-magnetic (EM) wave activity, or the Parker spiral, non-radial, magnetic field. It assumes spherically geometric radial expansion to reconstruct a 3-dimensions in space from its 1-dimensional simulation domain. However, it allows us to focus on electron kinetic physics on the global solar wind scales. Using this model we are able to quantify the contribution of the kinetic electron behavior, under the influence of gravity and Coulomb collisions, in the solar wind dynamics. As the resulting electron VDFs are not far from the observed ones, we can speculate that the recognised differences between the modeled and observed VDF are the result of the physical mechanisms not included in our simulation, like EM waves or non-radial magnetic field.

The simulation run A presents the solar wind arising solely from the hot Maxwellian solar corona with a temperature of 2 MK (172 eV). This temperature is higher than value 0.79 MK reported above the surface for the coronal holes (Cranmer, 2002; David et al., 1998), but an upper limit temperature related to the edges of coronal holes in the recent study by Berčič et al. (2020) inferring the temperature of the coronal electrons from the strahl electrons measured by PSP. The estimated density at 1 R_S in the simulation is about one order of magnitude lower than that reported for the coronal holes, measured by multi-frequency radio imaging (Mercier & Chambe, 2015). Due to their small mass, the contribution of electrons to the total mass flux of the solar wind is very small, however,

Figure 12. Electron VDFs, integrated along the $\perp$ direction ($f_\parallel$), for different radial bins, normalized with a Maxwellian VDF with the temperature $T_{e,\mathrm{bot}}$. X-axis represents velocity (v) multiplied with its absolute value in the units of square of thermal velocity of the electron VDF at the bottom boundary (w_0^2). Radial distance is presented in color spanning from blue closer to the Sun to red at the top boundary. Presented data is from the run MC, the same figures from runs HC and LC can be found in Appendix B. HC, high collisionality; LC, low collisionality; MC, medium collisionality; VDF, velocity distribution function.
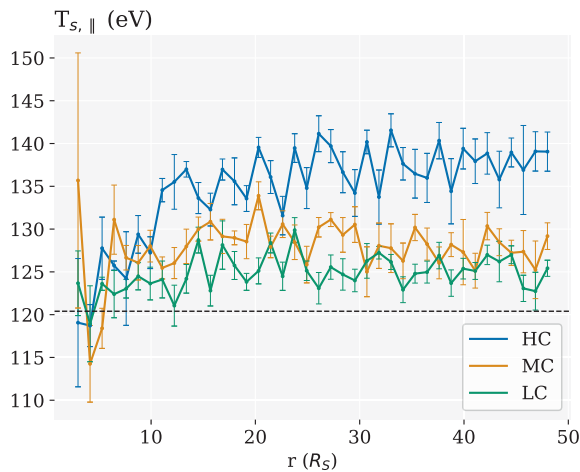
Figure 13. Evolution of $T_\parallel$ over radial distance for the simulation runs HC, MC, and LC. The dashed black line shows the temperature of the Maxwellian set at the bottom boundary. Error bars represent the standard error for Poisson counting ($\sqrt{N}$). HC, high collisionality; LC, low collisionality; MC, medium collisionality.

the high velocities they reach, and their subsonic behavior have an important role in the solar wind acceleration. In comparison to the heavier protons, electrons evaporate from the Sun faster, which requires an existence of large-scale electric field ensuring the plasma quasi-neutrality (Lemaire & Scherer, 1971). This electric field is referred to as the *ambipolar* electric field (E), and is self-consistently obtained in the simulation. It is responsible for acceleration of the solar wind protons to the supersonic velocity at 4 R_S, and to the terminal velocity of 206 km/s. Even though the modeled corona is somewhat hotter than measured, the obtained terminal velocity is still about a third smaller than frequently observed velocities of ∼300 km/s during the first two encounters of the PSP (Kasper et al., 2019). We conclude that the ambipolar electric field is an important driver of the solar wind acceleration, but can alone not produce the terminal velocities observed in the solar wind. A significant contribution could be due to the heat and momentum transfer from electro-magnetic wave activity and turbulence (Tu & Marsch, 1997, 2001). At the same time, the shape of the coronal particle VDFs has an important effect on the solar wind acceleration. For example, fast solar wind can be produced by the exospheric solar wind models assuming a Kappa electron VDF in the solar corona (Lamy et al., 2003; Maksimovic et al., 1997) even including the effect of binary particle collisions Zouganelis et al. (2005). Moreover, several evidence seem to indicate that the coronal plasma is not in a thermal equilibrium. Strong temperature anisotropies were observed in the VDFs of coronal ions (e.g., Kohl et al., 1998). Different temperatures and thermal anisotropies in the proton distribution function can have a strong effect on the velocity of the resulting solar wind. However, the study how the solar wind terminal velocity depends on the bottom boundary parameters is out of the scope of the current work.

Our obtained electron VDF are very similar to the ones measured during the first two encounters of PSP (Halekas et al., 2019). The observed core electron temperatures, between 30 and 40 eV, are slightly lower than the modeled ones at 35 R_S. The density estimated for the simulation run MC corresponds well to an average density observed (∼300 cm^{-3}), while the densities in runs HC and LC reach the high and low extremes, respectively (see Table 2). However, as shown in Section 3.1.1, the determination of physical unit density from the model is not simple and some errors can be expected. We assume an accuracy up to an order of magnitude on the obtained absolute value, and pay more attention to the relative values between the simulation runs. The biggest difference between the modeled and observed VDFs is that halo electron component is not present in the modeled one. This leads us to believe that the halo is an outcome of phenomena not included in the kinetic model and we can rule out the Coulomb collisions, and ambipolar electric field as possible halo generation mechanisms.

6.2. Ambipolar Electric Field

The electric field in the solar wind is responsible for the energy transfer from electrons to protons, modifying the fluid properties of the solar wind, like velocity and temperature, as well as the kinetic properties of electron VDF. Its cumulative effects explain the two-component form of electron VDF in the exospheric models (Jockers, 1970; Lemaire & Scherer, 1971). The total electric potential exerted on them by protons (through E) creates a potential well, at each radial distance separating electron VDF in two regimes. Electrons with anti-sunward velocities high enough to climb out of the potential well can escape and form the strahl. Electrons with anti-sunward velocities lower than that are ballistic. After they use all their energy they start falling back, forming the sunward directed part of electron VDF, symmetrical about $v = 0$ in Sun's resting frame. The ballistic population represents the electron core. In exospheric models the separation velocity (v_ϕ, Equation 11) defines two boundaries in electron VDF. In the anti-sunward direction, it separates the core and the strahl population, and in the sunward direction it defines the largest possible electron speed, referred to as the electron cutoff.

The strength and the radial evolution of the ambipolar potential are therefore closely related to the evolution of the core electron temperature, which has been observed to vary with radial distance as $\sim r^{-0.8}$ in the slow, and as $\sim r^{-0.3}$ in the fast solar wind (e.g., Štverák et al. (2015); Maksimovic et al. (2020)). This is much slower than the radial decrease of ambipolar potential obtained by collisionless exospheric models, $\sim r^{-4/3}$ (Meyer-Vernet & Issautier, 1998; Zouganelis et al., 2004). Accounting for Coulomb collisions, Boldyrev et al. (2020) (inspired by the earlier exospheric models of Jockers, 1970; Khazanov et al., 1998; Lamy et al., 2003; Zouganelis et al., 2004, and by the kinetic models of Dorelli & Scudder, 2003; Landi & Pantellini, 2003; Landi et al., 2012) analytically obtain that the electron core temperature and ambipolar potential evolve radially as $\sim r^{-0.4}$. This result compares well to the observations, and the evolution found from BiCoP simulations, $\sim r^{-0.5}$.

The behavior of a fully ionized gas under the influence of an electric field of arbitrary magnitude was studied by (Dreicer, 1959, 1960). He defined a parameter relating electric field strength to the collisionality, which is after him referred to as the *Dreicer electric field* (E_D, Equation 13). In a homogeneous plasma, an electric field of 0.43 E_D, causes electrons to drift with respect to the ions, with a velocity equal to their thermal velocity. For $E > E_D$, electrons efficiently gain energy in a process called *runaway*. This scenario, characterized by large electric currents, was observed in the fusion laboratory experiments. Scudder (1996) generalized the Dreicer's work to make it applicable to the solar wind, where zero current condition appears to be fulfilled despite the presence of ambipolar electric field (E) of the order of E_D. Analytically calculated E at the solar wind critical point was shown to be between 0.6 and 2 E_D. Following the work of Fuchs et al. (1986), he defines a boundary velocity (v_D, Equation 14), separating the electron velocity space into a region where E is overdamped by collisions, and a region where E is underdamped.

In the series of articles by Scudder (2019a, 2019b, 2019c), the author develops a Steady Electron Runaway Model (SERM) of the solar wind, based on the presence of E. In this model, all the suprathermal electrons, moving toward or away from the Sun, are a consequence of the runaway mechanism. The expected electron VDF is shown in Scudder (2019b)—Figure 4, where the boundary between the core and the suprathermal electrons in both parallel directions is v_D.

Two different solar wind models, provide two separation velocities. v_ϕ predicted by the exospheric models describes the effects of the electric potential, thus the cumulative effects of E. v_D from SERM model is a result of the local effects of E. v_ϕ in our simulations corresponds the cutoff velocity over all the simulation domain, while the strahl break point is well described by v_D. This is clearly visible in the least collisional run LC, where v_D is much lower than v_ϕ (see Figure 8d). In the anti-sunward direction v_ϕ still describes the properties of the core population, it marks the velocity at which the core electron flux strongly decreases.

We note that the sunward directed portion of the electron VDF had to be defined at the top boundary and was assumed to be Maxwellian. Any non-Maxwellian features injected at the top boundary are in the model propagated toward the Sun, accordingly with the separation velocity v_D. An example of a simulation run with a non-Maxwellian top boundary condition is shown in Appendix C. The feature is damped by collisions for velocities below v_D, and persists for velocities above this speed.

In the solar wind non-Maxwellian features could be produced locally through field-particle interactions, and be propagated toward the Sun. Another mechanism producing a bump in the sunward direction could be the focusing of the strahl in cases where $v_\phi > v_D$. When this condition is fulfilled, part of the strahl electrons has energy bellow the electric potential energy required to escape the Sun. This means that these electrons reach their maximal radial distance and then start falling back toward Sun. As the anti-sunward portion of the VDF below v_ϕ is non-Maxwellian, this could translate into a non-Maxwellian sunward potion as well.

6.3. Strahl Electron Focusing

High energy, anti-sunward moving strahl electrons are able to escape the collisional core and focus around the radial magnetic field. In a collisionless approximation, a simple model conserving magnetic moment and electron energy (Berčič et al., 2019—Equation 6), describes the evolution of electron VDF from the exobase, where the focusing begins, to the measuring point. Additional required input parameter is the potential difference between these two points in space ($\Delta\phi$).

The focusing taking place in the simulation accounts for two additional physical effects, compared to the simple collisionless model described above. The first difference is that the exobase is not limited to a single radial distance, and accounts for so called *multi-exobase* phenomena. In the simulations the strahl starts to form gradually, from the highest energy electrons, which are first able to avoid Coulomb collisions and focus, to the lower energy electrons following the decrease of v_D with radial distance. Therefore, strahl electrons with different energies have different exobase locations. However, v_D gradient is the highest close to the Sun, therefore the exobases of the majority of strahl electrons lie within a relatively small radial distance. From Figure 9, Figures A1 and A2 we conclude that majority of the strahl is formed within ∼20 R_S. A second phenomena included in the kinetic model are the Coulomb collisions which can, despite the Coulomb cross-section decrease with v^4, have some effect on the strahl electrons.

The results in Figure 11, show that the high energy strahl electrons are not affected by Coulomb collisions, as the same PAW values are found for the simulation runs HC, MC, and LC. For the low energy strahl electrons the effect of collisionality is reflected in the shape of the decreasing PAW with electron energy. In a collisionless model and in the least collisional simulation run LC, the transition between low strahl PAWs and core PAWs reaching over 180° (only PAW below 180° are shown in Figure 11) is abrupt. While the collisions in run HC make this transition gradual and smooth, comparing better with the PAWs observed by PSP.

PAWs obtained from a single-exobase collisionless model with the exobase of 3 R_S do not compare well with PAWs measured for the collisionless, high-energy electrons in all three simulation runs, as well starting from 3 R_S. This difference is accounted to the multi-exobase phenomena. Furthermore, we found that exobase in the simple model needs to be shifted to 10 R_S, to correspond to the collisionless part of the strahl obtained by simulations BiCoP.

PAWs measured during the first two encounters of PSP, shown by Berčič et al. (2020) for the low electron beta solar wind, still appear from 10 to 20° wider than PAWs obtained in the most collisional simulation run HC. Since the gradual transition between core and strahl electrons is very similar to our simulation result we conclude that the difference is not a consequence of Coulomb collisions. We suggest that broader strahls observed by PSP are a result of the non-radial magnetic field topology not captured by our kinetic model, or a consequence of the measurement technique, integrating electron VDF over time periods with varying magnetic field angle. In fact, in-situ measured PAWs for energies above 300 eV were found to be between 10 and 15° larger for the instances during which the standard deviation of B was above 10 nT, than when it was below that value (Berčič et al., 2020).

The wider strahls observed could also result from scattering by EM fluctuations, however, due to the monotonic decreasing relation between strahl PAW and energy, some of scattering mechanisms can be ruled out. Scattering through a resonance with a whistler wave, for example, is expected to produce a peak in PAW at the resonant electron energy (Behar et al., 2020). And an electron VDF relaxation mechanism giving energy to a whistler wave would first scatter the higher energy strahl electrons, which would result in an increasing trend between PAW and energy (Verscharen et al., 2019). The inclusion of wave-particle interaction in BiCoP would be difficult, and would mean going back to the beginning of the code development. However, the effects of EM waves could be investigated otherwise. One could use the electron VDFs obtained by BiCoP and verify when they become unstable to kinetic instabilities. Another option would be to introduce an additional energy dependent scattering of the electrons corresponding to scattering by whistler turbulence.

The simple, single-exobase focusing model does not affect the parallel profile of the electron distribution function, therefore preserving its shape from the solar corona to the measuring point (Feldman et al., 1975). This argument was used by Berčič et al. (2020), who use the strahl parallel temperature ($T_{s,\parallel}$, Equation 16) measured by the PSP, to make a zero order estimation of the electron temperature in the solar corona. Surprisingly, $T_{s,\parallel}$ was found to increase with radial distance in our simulation runs. The smallest increase was found for the least collisional run LC amounting to only 3%, while the $T_{s,\parallel}$ in the most collisional run HC increased for 15%. Due to the correlation between the percentage of increase in $T_{s,\parallel}$ and the collisionality of the system, we believe the effective heating of the strahl electrons is caused by Coulomb collisions.

With a schematics in Figure 14, we propose a physical mechanism which could result in an increase of $T_{s,\parallel}$ with radial distance. The parallel cut through electron VDF is illustrated with straight lines in the logarithmic parameter space, representing Maxwellians with different temperatures. Figure 14a shows the
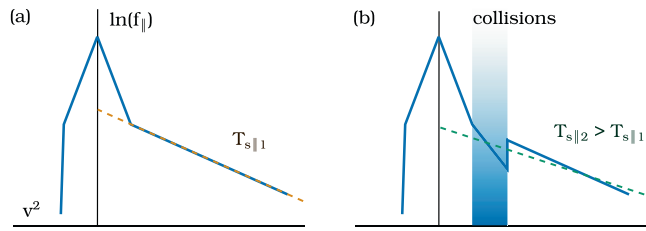
Figure 14. An illustration of how Coulomb collisions can increase $T_{s,\parallel}$. (a) Collisionless case, (b) collisions decrease the temperature of only lowest energy strahl electrons, which results in the increase of the total effective $T_{s,\parallel}$.

core and the strahl for a collisionless case, where a yellow dashed line represents the fit giving $T_{s,\parallel}$. The same VDF cut is shown in Figure 14b for a collisional case, where the lowest strahl energies are affected by Coulomb collisions. In the region marked with blue, the strahl electrons are cooled down by collisions, however, when fitting to the whole strahl energy range (green dashed line), the obtained temperature is higher than the one obtained for the collisionless case (a). In the simulation this mechanism, exaggerated in the schematics, is continuous, reshaping the the parallel cut through the strahl VDF over the radial distance. The strahl parallel profiles obtained by the kinetic model are well represented by a Maxwellian, however, it is not obvious why a mechanism described above would preserve a Maxwellian shape.

Comparing the simulation results with the observations shown by Berčič et al. (2020), we believe that most of the solar wind observed during the first two encounters of PSP best corresponds to the simulation runs HC or MC. Therefore the presented $T_{s,\parallel}$ (Berčič et al. (2020)—Figures 6 and 7) probably overestimates the temperature of coronal electrons. In the simulation runs HC and MC at the distance of ~35 R_S, $T_{s,\parallel}$ is overestimated by 15% and 8%, respectively. Applying this correction to the observed $T_{s,\parallel}$ with a mean value of 96 eV, we obtain the mean temperature of coronal electrons between 83 and 89 eV.

7. Conclusions

We presented results of a kinetic model of the solar wind accounting for BiCoP, simulating the solar wind acceleration region (1–45 R_S). The model does not include EM waves and non-radial magnetic fields. Nevertheless, it can produce a solar wind, accelerated only through the ambipolar electric field (E), rising from the difference in the pressure gradients between electrons and protons. High coronal temperatures were assumed, leading to the terminal solar wind velocities approximately a third smaller than the ones reported by PSP. We conclude that, while E is responsible for a big part of solar wind terminal velocity, it is not the only solar wind acceleration mechanism.

The self-consistently obtained E in our model was found to be on the order of the Dreicer electric field (E_D). We analyzed the effects it has on electron VDF. The cumulative effects of E were predicted by exospheric solar wind models, and the separation velocity v_ϕ correlates well with the electron sunward cutoff velocity. Similarly, v_ϕ describes an upper velocity limit for the core population in the anti-sunward direction. The local effects of E on the VDF were described by the SERM (Scudder, 2019b) predicting a separation of electron velocity space into two regions separated by v_D: an overdamped region, where collisions are frequent enough to overdamp the electric force and preserve a Maxwellian VDF, and an underdamped region, where electrons can be accelerated by E and departures from a Maxwellian VDF can be found. In our obtained VDFs v_D represents well the strahl break point velocity.

Strahl focusing in the kinetic model is compared to the simple, single-exobase collisionless focusing model. We find that at the distance of 34 R_S, energies above 250 eV are not affected by Coulomb collisions. Pitch-angle widths are observed to be larger than the ones obtained from a simple focusing model, and this difference is accounted to the multi-exobase phenomena. For energies below 250 eV Coulomb collisions are able to scatter the strahl electrons and change the dependence of PAW on electron energy.

In the collisionless approximation the strahl parallel temperature ($T_{s,\parallel}$) is independent of radial distance. However, $T_{s,\parallel}$ in our simulation runs was found to be larger than the temperature set at the bottom boundary, and the increase to be correlated to the collisionality of the system. We presented a raw idea of how scattering of the low energy strahl electrons by Coulomb collisions in the solar wind acceleration region could affect $T_{s,\parallel}$.

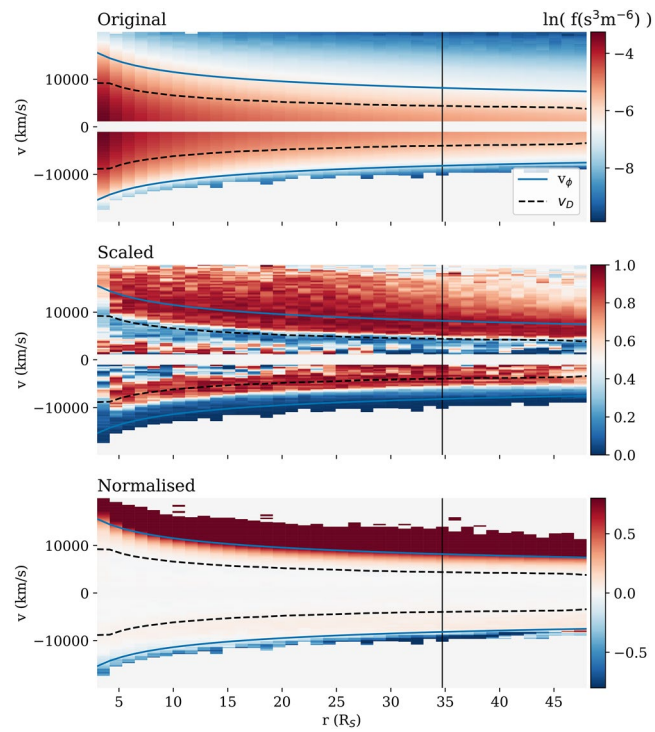## Appendix A: Radial Evolution of the Parallel Cuts Through Electron VDF for Simulation Runs HC and LC

Figure A1. Parallel cuts through electron VDF plotted with respect to the radial distance in original (top), scaled (middle), and normalised (bottom) representation for the simulation run HC. v_ϕ and v_D are marked with blue and black lines. A black vertical line denotes the radial distance of the VDFs shown in Figure 8c. VDF, velocity distribution function.

Figure A2. Parallel cuts through electron VDF plotted with respect to the radial distance in original (top), scaled (middle), and normalised (bottom) representation for the simulation run LC. v_ϕ and v_D are marked with blue and black lines. A black vertical line denotes the radial distance of the VDFs shown in Figure 8d. VDF, velocity distribution function.
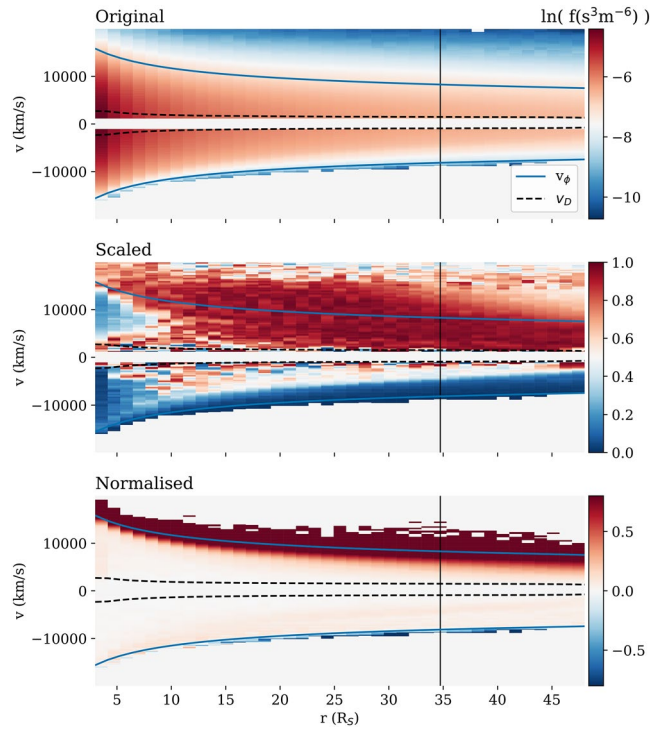
Appendix B: $f_\parallel$ Normalised to the Maxwellian at the Bottom Boundary for Simulation Runs HC and LC
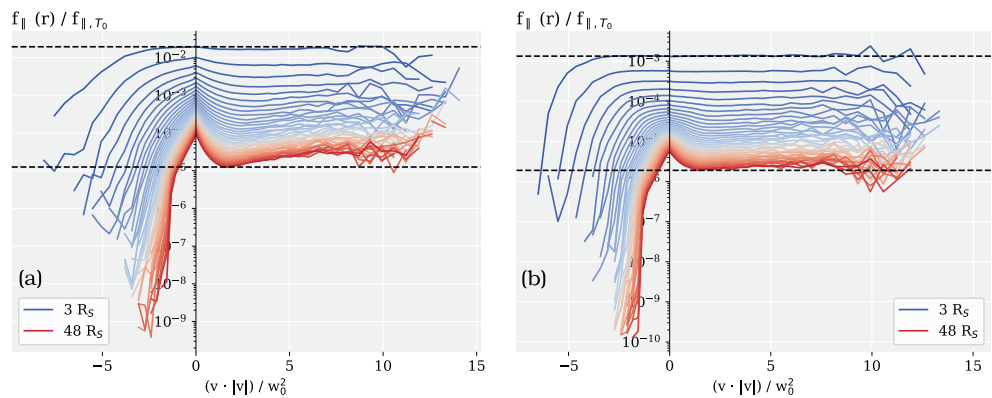

Figure B1. Electron VDFs, integrated along the $\perp$ direction ($f_\parallel$), for different radial bins, normalised with a Maxwellian VDF with the temperature $T_{e,\text{bot}}$. X-axis represents velocity (v) multiplied with its absolute value in the units of square of thermal velocity of the electron VDF at the bottom boundary (w_0^2). Radial distance is presented in color spanning from blue closer to the Sun to red at the top boundary. Presented data is from the run HC (left) and run LC (right). VDF, velocity distribution function.

Appendix C: Simulation Run With a Non-Maxwellian Top Boundary Condition

With slices through electron VDFs at different radial distances we demonstrate the propagation of the non-Maxwellian feature produced in the sunward portion of the electron VDF at the top boundary. The parameters used for the presented run are gathered in Table C1. In this simulation run, v_D (black dashed line
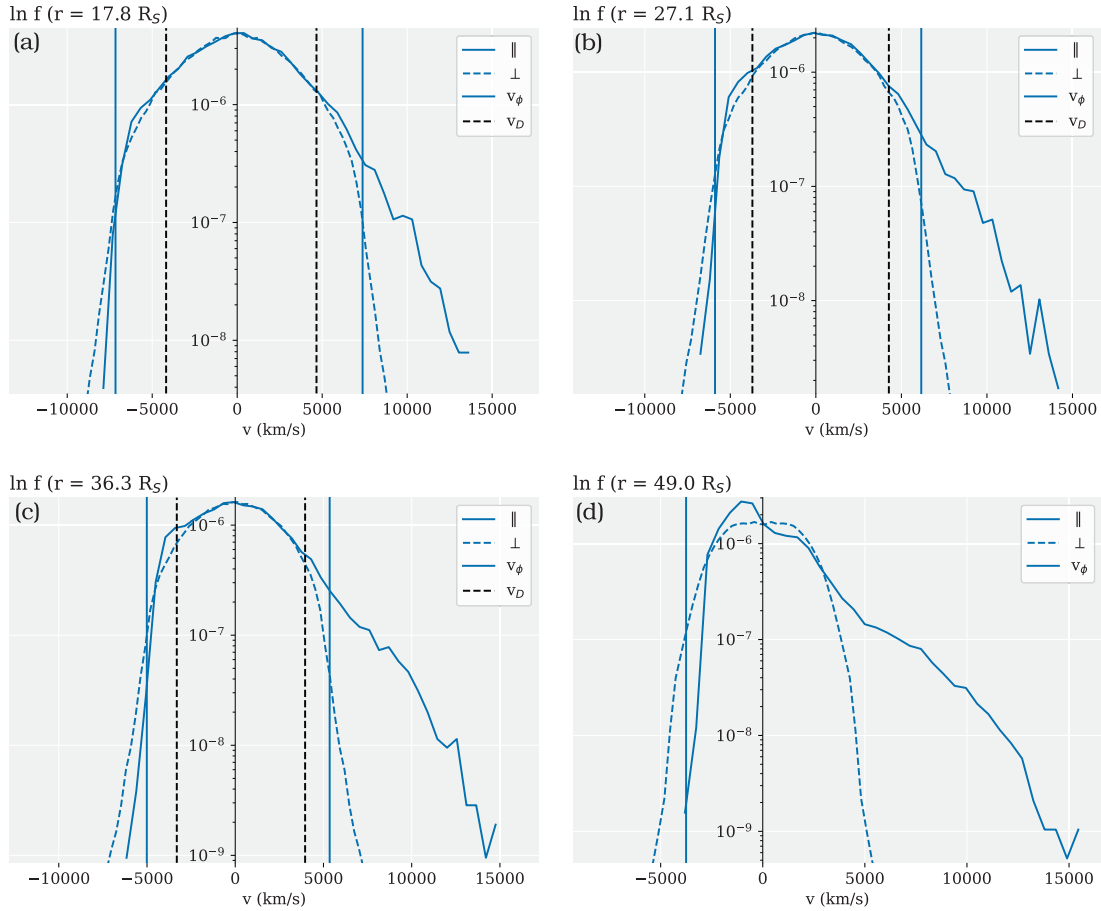

Figure C1. Parallel and perpendicular cuts through electron VDF, at different radial distances (marked in the title of each plot) for the simulation run with a non-Maxwellian top boundary condition. The electric potential velocity (v_ϕ) and the Dreicer velocity (v_D) are marked with blue and black lines. VDF, velocity distribution function.

Table C1
Presented Simulation Runs And Their Crucial Input Parameters

Parameters	Unit	Non-Maxw.
N		22,500
v_C	$v_{th,0}$	0.3
$T_{e,p,bot}$	10^6 K	1
$T_{e,top}$	10^6 K	0.4
g_0		0.0177
r	R_S	4–49
v_{bot}	km/s	77
v_{top}	km/s	171

in Figure C1) separates the over-, and underdamped parts of the VDF in both directions. In the antisunward direction it marks the beginning of the strahl component, as already shown for runs HC, MC, and LC. In the sunward direction v_D follows the beginning of the feature propagating toward the Sun, separating electron VDF into Maxwellian and non-Maxwellian parts.

Data Availability Statement

The simulation data used in this work are publicly available: HC run (https://doi.org/10.6084/m9.figshare.13160114.v1), MC run (https://doi.org/10.6084/m9.figshare.13160132.v1), and LC run (https://doi.org/10.6084/m9.figshare.13160102.v1).

References

Behar, E., Sahraoui, F., & Beri, L. (2020). Resonant whistler-electron interactions: Mms observations versus test-particle simulation. *Journal of Geophysical Research: Space Physics*, *125*(10), e2020JA028040. https://doi.org/10.1029/2020JA028040

Berčič, L., Maksimović, M., Landi, S., & Matteini, L. (2019). Scattering of strahl electrons in the solar wind between 0.3 and 1 au: Helios observations. *Monthly Notices of the Royal Astronomical Society*, *486*(3), 3404–3414. https://doi.org/10.1093/mnras/stz1007

Berčič, L., Larson, D., Whittlesey, P., Maksimović, M., Badman, S. T., Landi, S., et al. (2020). Coronal electron temperature inferred from the strahl electrons in the inner heliosphere: *Parker Solar Probe and Helios Observations*, *892*(2), 88. https://doi.org/10.3847/1538-4357/ab7b7a

Boldyrev, S., Forest, C., & Egedal, J. (2020). Electron temperature of the solar wind. *Proceedings of the National Academy of Sciences*, *117*(17), 9232–9240. https://doi.org/10.1073/pnas.1917905117

Boldyrev, S., & Horaites, K. (2019). Kinetic theory of the electron strahl in the solar wind. *Monthly Notices of the Royal Astronomical Society*, *489*(3), 3412–3419. https://doi.org/10.1093/mnras/stz2378

Brasseur, G., & Lemaire, J. (1977). Fitting of hydrodynamic and kinetic solar wind models. *Planetary and Space Science*, *25*(2), 201–203. https://doi.org/10.1016/0032-0633(77)90028-9

Chamberlain, J. W. (1960). Interplanetary Gas.II. Expansion of a Model Solar Corona. *Astrophysical Journal*, *131*, 47. https://doi.org/10.1086/146805

Cranmer, S. (2002). *Coronal holes and the solar wind COSPAR Colloquia series (January)*, *1–10*. https://doi.org/10.1016/S0964-2749(02)80003-8

David, C., Gabriel, A. H., Bely-Dubau, F., Fludra, A., Lemaire, P., & Wilhelm, K. (1998). Measurement of the electron temperature gradient in a solar coronal hole. *Astronomy and Astrophysics*, *336*(3), 90–94.

Dorelli, J., & Scudder, J. (2003). A new look at electron heat flow in the solar corona. In *Egs—agu—eug joint assembly* (p. 7358).

Dreicer, H. (1959). Electron and ion runaway in a fully ionized gas. I. *Physical Review*, *115*(2), 238–249. https://doi.org/10.1103/PhysRev.115.238

Dreicer, H. (1960). Electron and ion runaway in a fully ionized gas. II. *Physical Review*, *117*(2), 329–342. https://doi.org/10.1103/PhysRev.117.329

Feldman, W. C., Asbridge, J. R., Bame, S. J., Montgomery, M. D., & Gary, S. P. (1975). Solar wind electrons. *Journal of Geophysical Research*. https://doi.org/10.1029/JA080i031p04181

Fox, N. J., Velli, M. C., Bale, S. D., Decker, R., Driesman, A., Howard, R. A., et al. (2016). The solar probe plus mission: Humanity's first visit to our star. *Space Science Reviews*, *204*(1–4), 7–48. https://doi.org/10.1007/s11214-015-0211-6

Fuchs, V., Cairns, R. A., Lashmore-Davies, C. N., & Shoucri, M. M. (1986). Velocity-space structure of runaway electrons. *Physics of Fluids*, *29*(9), 2931–2936. https://doi.org/10.1063/1.865493

Graham, G. A., Rae, I. J., Owen, C. J., Walsh, A. P., Arridge, C. S., Gilbert, L., et al. (2017). The evolution of solar wind strahl with heliospheric distance. *Journal of Geophysical Research: Space Physics*, *122*(4), 3858–3874. https://doi.org/10.1002/2016JA023656

Halekas, J. S., Whittlesey, P., Larson, D. E., Mcginnis, D., Maksimović, M., Berthomier, M., et al. (2019). Electrons in the young solar wind: First results from parker solar probe. *The Astrophysical Journal*. https://doi.org/10.3847/1538-4365/ab4cec

Hammond, C. M., Feldman, W. C., McComas, D. J., Phillips, J. L., & Forsyth, R. J. (1996). Variation of electron-strahl width in the high-speed solar wind: ULYSSES observations. *Astronomy and Astrophysics*, *316*, 350–354. Retrieved from http://ukads.nottingham.ac.uk/abs/1996A&A...316.350H

Hefti, S., Zurbuchen, T. H., Fisk, L. A., Gloeckler, G., Larson, D., & Lin, R. P. (1999). The transition from slow to fast solar wind: Charge state composition and electron observations. *AIP Conference Proceedings*, *471*, 495. https://doi.org/10.1063/1.58682

Held, E. D., Callen, J. D., & Hegna, C. C. (2003). Conductive electron heat flow along an inhomogeneous magnetic field. *Physics of Plasmas*, *10*(10), 3933–3938. https://doi.org/10.1063/1.1611883

Horaites, K., Boldyrev, S., & Medvedev, M. V. (2019). Electron strahl and halo formation in the solar wind. *Monthly Notices of the Royal Astronomical Society*, *484*(2), 2474–2481. https://doi.org/10.1093/mnras/sty3504

Horaites, K., Boldyrev, S., Wilson, L. B., Viñas, A. F., & Merka, J. (2018). Kinetic theory and fast wind observations of the electron strahl. *Monthly Notices of the Royal Astronomical Society*, *474*(1), 115–127. https://doi.org/10.1093/MNRAS/STX2555

Jagarlamudi, V. K., Alexandrova, O., Berčič, L., de Wit, T. D., Krasnoselskikh, V., Maksimović, M., & Štverák, Š. (2020). Whistler waves and electron properties in the inner heliosphere: Helios observations. *The Astrophysical Journal*, *897*(2), 118. https://doi.org/10.3847/1538-4357/ab94a1

Jockers, K. (1970). Solar wind models based on exospheric theory. *Astronomy and Astrophysics*, *6*(219). Retrieved from https://ui.adsabs.harvard.edu/abs/1970A&A...6.219J

Kajdič, P., Alexandrova, O., Maksimović, M., Lacombe, C., & Fazakerley, A. N. (2016). Suprathermal electron strahl widths in the presence of narrow-band whistler waves in the solar wind. *The Astrophysical Journal*, *833*(2), 172. https://doi.org/10.3847/1538-4357/833/2/172

Kasper, J. C., Bale, S. D., Belcher, J. W., Berthomier, M., Case, A. W., Chandran, B. D. G., et al. (2019). Alfvénic velocity spikes and rotational flows in the near-Sun solar wind. *Nature*, *576*(7786), 228–231. https://doi.org/10.1038/s41586-019-1813-z

Khazanov, G. V., Liemohn, M. W., Krivorutsky, E. N., & Moore, T. E. (1998). Generalized kinetic description of a plasma in an arbitrary field-aligned potential energy structure. *Journal of Geophysical Research*, *103*(A4), 6871–6890. https://doi.org/10.1029/97JA03436

Kohl, J. L., Noci, G., Antonucci, E., Tondello, G., Huber, M. C. E., Cranmer, S. R., et al. (1998). UVCS/SOHO empirical determinations of anisotropic velocity distributions in the solar corona. *The Astrophysical Journal*, *501*(1), L127–L131. https://doi.org/10.1086/311434

Lamy, H., Pierrard, V., Maksimovic, M., & Lemaire, J. F. (2003). A kinetic exospheric model of the solar wind with a nonmonotonic potential energy for the protons. *Journal of Geophysical Research*, *108*(A1), 1047. https://doi.org/10.1029/2002JA009487

Landi, S., Matteini, L., & Pantellini, F. (2012). On the competition between radial expansion and Coulomb collisions in shaping the electron velocity distribution function: Kinetic simulations. *Astrophysical Journal*, *760*(2). https://doi.org/10.1088/0004-637X/760/2/143

Landi, S., Matteini, L., & Pantellini, F. (2014). Electron heat flux in the solar wind: Are we observing the collisional limit in the 1 AU data? *Astrophysical Journal Letters*, *790*(1), 1–5. https://doi.org/10.1088/2041-8205/790/1/L12

Landi, S., & Pantellini, F. (2001). On the temperature profile and heat flux in the solar corona: Kinetic simulations. *Astronomy & Astrophysics*, *372*, 686–701. https://doi.org/10.1051/0004-6361:20010552

Landi, S., & Pantellini, F. (2003). Kinetic simulations of the solar wind from the subsonic to the supersonic regime. *Astronomy and Astrophysics*, *400*, 769–778. https://doi.org/10.1051/0004-6361:20021822

Landi, S., Pantellini, F., & Matteini, L. (2010). Radial evolution of the electron velocity distribution in the heliosphere: Role of collisions. *AIP Conference Proceedings*, *1216*(1), 218–222. https://doi.org/10.1063/1.3395841

Lemaire, J., & Scherer, M. (1970). Model of the polar ion-exosphere. *Planetary and Space Science*, *18*(1), 103–120. https://doi.org/10.1016/0032-0633(70)90070-X

Lemaire, J., & Scherer, M. (1971). Kinetic models of the solar wind. *Journal of Geophysical Research*, *76*, 7479. https://doi.org/10.1029/JA076i031p07479

Lie-Svendsen, Ø., & Leer, E. (2000). The electron velocity distribution in the high-speed solar wind: Modeling the effects of protons. *Journal of Geophysical Research*, *105*(A1), 35–46. https://doi.org/10.1029/1999JA900438

MacNeil, A. R., Owen, C. J., & Wicks, R. T. (2017). Tests for coronal electron temperature signatures in suprathermal electron populations at 1 AU. *Annales Geophysicae*, *35*(6), 1275–1291. https://doi.org/10.5194/angeo-35-1275-2017

Macneil, A. R., Owens, M. J., Lockwood, M., Štverák, Š., & Owen, C. J. (2020). Radial evolution of sunward strahl electrons in the inner heliosphere. *Solar Physics*, *295*(2), 16. https://doi.org/10.1007/s11207-019-1579-3

Maksimovic, M., Bale, S. D., Berčič, L., Bonnell, J. W., Case, A. W., Dudok de Wit, T., et al. (2020). Anticorrelation between the bulk speed and the electron temperature in the pristine solar wind: First results from the parker solar probe and comparison with Helios. *Astrophysical Journal*, *246*(2), 62. https://doi.org/10.3847/1538-4365/ab61fc

Maksimovic, M., Pierrard, V., & Lemaire, J. F. (1997). A kinetic model of the solar wind with Kappa distribution functions in the corona. *Astronomy and Astrophysics*, *324*, 725–734.

Maksimovic, M., Zouganelis, I., Chaufray, J. Y., Issautier, K., Scime, E. E., Littleton, J. E., et al. (2005). Radial evolution of the electron distribution functions in the fast solar wind between 0.3 and 1.5 AU. *Journal of Geophysical Research*, *110*(A9), 1–9. https://doi.org/10.1029/2005JA011119

Mercier, C., & Chambe, G. (2015). Electron density and temperature in the solar corona from multifrequency radio imaging (583, p. A101). https://doi.org/10.1051/0004-6361/201425540

Meyer-Vernet, N., & Issautier, K. (1998). Electron temperature in the solar wind: Generic radial variation from kinetic collisionless models. *Journal of Geophysical Research*, *103*(A12), 29705–29718. https://doi.org/10.1029/98JA02853

Pagel, C., Gary, S. P., de Koning, C. A., Skoug, R. M., & Steinberg, J. T. (2007). Scattering of suprathermal electrons in the solar wind: ACE observations. *Journal of Geophysical Research*, *112*(A4), 1–11. https://doi.org/10.1029/2006JA011967

Pannekoek, A. (1922). Ionization in stellar atmospheres (Errata: 2 24). *Bulletin of the Astronomical Institutes of the Netherlands*, *1*, 107.

Parker, E. N. (1958). Dynamics of the interplanetary gas and magnetic fields. *The Astrophysical Journal*, *128*, 664. https://doi.org/10.1086/146579

Pierrard, V., Maksimovic, M., & Lemaire, J. (1999). Electron velocity distribution functions from the solar wind to the corona. *AIP Conference Proceedings*, *104*(A8), 17021–17032. https://doi.org/10.1029/1999JA900169

Pilipp, W. G., Miggenrieder, H., Montgomery, M. D., Mühlhäuser, K. H., Rosenbauer, H., & Schwenn, R. (1987). Characteristics of electron velocity distribution functions in the solar wind derived from the Helios Plasma Experiment. *Journal of Geophysical Research*, *92*(A2), 1075. Retrieved from http://doi.wiley.com/10.1029/JA092iA02p01075

Rosseland, S. (1924). Electrical state of a star. *Monthly Notices of the Royal Astronomical Society*, *84*, 720–728. https://doi.org/10.1093/mnras/84.9.720

Saito, S., & Gary, P. S. (2007). All whistlers are not created equally: Scattering of strahl electrons in the solar wind via particle-in-cell simulations. *Geophysical Research Letters*, *34*(1), 1–5. https://doi.org/10.1029/2006GL028173

Salem, C., Hubert, D., Lacombe, C., Bale, S. D., Mangeney, A., Larson, D. E., & Lin, R. P. (2003). Electron properties and Coulomb collisions in the solar wind at 1 AU. *Wind Observations*, *585*(2), 1147–1157. https://doi.org/10.1086/346185

Scudder, J. D. (1996). Dreicer order ambipolar electric fields at Parker's steady state solar wind sonic critical point. *Journal of Geophysical Research*, *101*(A6), 13461–13472. https://doi.org/10.1029/96JA00189

Scudder, J. D. (2019a). The long-standing closure crisis in coronal plasmas. *The Astrophysical Journal*, *885*(2), 148. https://doi.org/10.3847/1538-4357/ab48e0

Scudder, J. D. (2019b). Steady electron runaway model SERM. *Astrophysical Alternative for the Maxwellian Assumption*, *885*(2), 138. https://doi.org/10.3847/1538-4357/ab4882

Scudder, J. D. (2019c). The thermal force in astrophysical plasmas: Current free Coulomb friction. *The Astrophysical Journal*, *882*(2), 146. https://doi.org/10.3847/1538-4357/ab3348

Smith, H. M., Marsch, E., & Helander, P. (2012). Electron transport in the fast solar wind. *The Astrophysical Journal*, *753*(1), 31. https://doi.org/10.1088/0004-637X/753/1/31

Štverák, Š., Maksimovic, M., Trávníček, P. M., Marsch, E., Fazakerley, A. N., & Scime, E. E. (2009). Radial evolution of nonthermal electron populations in the low-latitude solar wind: Helios, Cluster, and Ulysses Observations. *Journal of Geophysical Research*, *114*(5), 1–15. https://doi.org/10.1029/2008JA013883

Štverák, Š., Trávníček, P. M., & Hellinger, P. (2015). Electron energetics in the expanding solar wind via Helios observations. *Journal of Geophysical Research*, *120*(10), 8177–8193. https://doi.org/10.1002/2015JA021368

Stverak, ˇS., Tr´avn´ıˇcek, P., Maksimovic, M., Marsch, E., Fazakerley, A. N., & Scime, E. E. (2008). Electron temperature anisotropy constraints in the solar1017 wind. *Journal of Geophysical Research*, *113*(A3), A03103. https://doi.org/10.1029/2007JA0127331019

Tang, B., Zank, G. P., & Kolobov, V. (2018). Numerical modeling of electron transport in solar wind: Effects of whistler turbulence and Coulomb collisions. *Journal of Physics Conference Series*, *1100*, 012025. https://doi.org/10.1088/1742-6596/1100/1/012025

Tao, J., Wang, L., Zong, Q., Li, G., Salem, C. S., Wimmer-Schweingruber, R. F., et al. (2016). Quiet-time suprathermal (˜0.1-1.5 keV) electrons in the solar wind. *The Astrophysical Journal*, *820*(1), 22. https://doi.org/10.3847/0004-637X/820/1/22

Tu, C. Y., & Marsch, E. (1997). Two-fluid model for heating of the solar corona and acceleration of the solar wind by high-frequency alfven waves. *Solar Physics*, *171*(2), 363–391. https://doi.org/10.1023/A:1004968327196

Tu, C. Y., & Marsch, E. (2001). On cyclotron wave heating and acceleration of solar wind ions in the outer corona. *Journal of Geophysical Research*, *106*(A5), 8233–8252. https://doi.org/10.1029/2000JA000024

Verscharen, D., Chandran, B. D. G., Jeong, S.-Y., Salem, C. S., Pulupa, M. P., & Bale, S. D. (2019). Self-induced scattering of strahl electrons in the solar wind. *The Astrophysical Journal*, *886*(2), 136. https://doi.org/10.3847/1538-4357/ab4c30

Vocks, C., Salem, C., Lin, R. P., & Mann, G. (2005). Electron halo and strahl formation in the solar wind by resonant interaction with whistler waves. *The Astrophysical Journal*, *627*(1), 540–549. https://doi.org/10.1086/4301191015

Wilson, I., Lynn, B., Chen, L.-J., Wang, S., Schwartz, S. J., Turner, D. L., et al. (2019a). Electron energy partition across interplanetary shocks. II. *Statistics*, *245*(2), 24. https://doi.org/10.3847/1538-4365/1022ab54451023

Wilson, I., Lynn, B., Chen, L.-J., Wang, S., Schwartz, S. J., Turner, D. L., et al. (2019b). Electron energy partition across interplanetary shocks. I. *Methodology and Data Product.*, *243*(1), 8. https://doi.org/10.3847/1538-4365/ab22bd1027

Zouganelis, I., Maksimovic, M., Meyer-Vernet, N., Lamy, H., & Issautier, K. (2004). A transonic collisionless model of the solar wind. *The Astrophysical Journal*, *1029* 606, 542–554. https://doi.org/10.1086/3828661031

Zouganelis, I., Meyer-Vernet, N., Landi, S., Maksimovic, M., & Pantellini, F. (2005). Acceleration of weakly collisional solar-type winds. *The Astrophysical Journal*, *626*(2), L117–L120. https://doi.org/10.1086/4319041034